

NPS ARCHIVE  
1964  
BEARD, P.

Library  
U. S. Naval Postgraduate School  
Monterey, California

DUDLEY KNOX LIBRARY  
U. S. NAVAL POSTGRADUATE SCHOOL  
MONTEREY, CA 94062-5001









A HIGH RESOLUTION STUDY OF THE  $O^{18}(p,n)F^{18}$  REACTION

by

Percy Morris Beard, Jr.

Department of Physics  
Duke University





ABSTRACT

(Physics)

A HIGH RESOLUTION STUDY OF THE  $O^{18}(p,n)F^{18}$  REACTION

by

Percy Morris Beard, Jr.

Department of Physics  
Duke University

Date: \_\_\_\_\_

Approved:

\_\_\_\_\_  
Henry W. Newson, Supervisor

\_\_\_\_\_  
\_\_\_\_\_  
\_\_\_\_\_  
\_\_\_\_\_

An abstract of a dissertation submitted in partial  
fulfillment of the requirements for the degree  
of Doctor of Philosophy in the Department  
of Physics in the Graduate School of  
Arts and Sciences of  
Duke University

1964



## ABSTRACT

### A HIGH RESOLUTION STUDY OF THE $O^{18}(p,n)F^{18}$ REACTION

by

Percy Morris Beard, Jr.

A gas handling and recovery system has been developed for use in conjunction with the windowless cryogenic gas target chamber. It permits the employment of a limited quantity of rare gas where, during each run, the entire amount is cycled through the target chamber and then recovered with a minimum of loss or contamination.

Using a liter (NTP) of oxygen gas, 65% enriched in  $O^{18}$ , the relative total yield of the  $O^{18}(p,n)$  reaction was studied from threshold to 3.290 MeV proton energy. With a total effective proton energy spread of about 1/11000, a previously unreported resonance was observed and improved values of widths and energies were obtained for the other resonances. Through a method by which neutron and proton energies are measured simultaneously a Q-value for the reaction was determined at  $-2439 \pm 1.0$  keV which places threshold at  $2576 \pm 1.0$  keV.



In addition,  $O^{18}(p,n)$  neutrons were used in a series of transmission measurements to test the resolution capability of the gas target as a neutron source. Results were in general agreement with resolution predictions. Total neutron energy spreads were 250 eV and 500 eV at neutron energies of 30 keV and 525 keV respectively.

In view of the successful performance of the  $O^{18}(p,n)$  gas target, the feasibility of using a  $T^3(p,n)$  gas target as a neutron source is discussed.



## ACKNOWLEDGEMENTS

I am indebted to the United States Navy for its support of my work at Duke University. This dissertation is the result of my participation in the Navy's Junior Line Officer Advanced Scientific Educational Program.

To my immediate predecessor, Dr. Paul B. Parks, I must express sincere thanks and appreciation for his initial help in this project as well as for his continued assistance and useful advice. I am equally indebted to Dr. Edward G. Bilpuch for his encouragement, guidance, and invaluable assistance in the laboratory and to Dr. H.W. Newson for his stimulating interest in and continuing support of my work. To all other members of the Nuclear Structure Laboratory lending their time and help to my cause I am truly grateful.

In addition I express my gratitude to Mr. Milton Whitfield and the Duke University Instrument Shop for their close cooperation in the fabrication of experimental apparatus. In particular I would like to thank Mr. Alton Lovette for his keen interest and outstanding work in the solution of my design problems. I also want to thank Mrs. Joseph R. Bailey for her long hours spent in making excellent drawings on my behalf.

Finally to Barbara who aided immensely in the initial typing and correction of this dissertation and who has faithfully withstood the rigors





of a graduate student's wife I extend my deepest appreciation.

This work was supported in part by the U.S. Atomic Energy Commission.



## CONTENTS

ABSTRACT	ii
ACKNOWLEDGEMENTS	iv
LIST OF FIGURES	viii
LIST OF TABLES	x
I. INTRODUCTION	2
II. APPARATUS	6
III. EXPERIMENTAL CONDITIONS AND PROCEDURE	20
A. Total Yield Measurement, 20	
B. Transmission Measurements, 29	
IV. DISCUSSION OF RESULTS	40
A. $O^{18}(p,n)F^{18}$ Cross Section, 40	
B. Neutron Transmission Measurements at $20^{\circ}$ , 51	
1. Q-value Determination, 51	
2. Neutron Energy Resolution, 57	
C. Neutron Transmission Measurements at $160^{\circ}$ , 67	
V. CONCLUSIONS	76



## APPENDIXES

82

A. Rare Gas Handling and Recovery System, 82

B. Operation of the Cryogenic Target Chamber, 95

C. Neutron Energy Resolution Calculations, 111

## LIST OF REFERENCES

124



## LIST OF FIGURES

1. Cryogenic Gas Target System	8
2. Cryogenic Target Chamber (Enlarged View)	10
3. Rare Gas Handling and Recovery System Table	15
4. Liquid Helium Trap (Enlarged View)	18
5. Experimental Floor Plan	22
6. $A^{40}(p,n)$ Resonance at 2.436 MeV	25
7. Relative Position of Target Chamber and Neutron Collimator	32
8. Proton Collimator Assembly ( $160^\circ$ Work)	37
9. $O^{18}(p,n)F^{18}$ Relative Total Yield	42
10. $O^{18}(p,n)F^{18}$ Relative Total Yield	44
11. $O^{18}(p,n)F^{18}$ Relative Total Yield	46
12. Neutron Transmissions in Natural Strontium	54
13. Neutron Transmissions in Natural Strontium	56
14. Neutron Transmissions in Natural Potassium	59





15. Neutron Transmissions in Natural Iron	61
16. Neutron Transmissions in Cobalt	69
17. Neutron Transmissions in Yttrium	71
18. Summary of Neutron Energy Resolution in the keV Region	78
19. Rare Gas Handling and Recovery System Diagram	84
20. Gas Reservoir	87
21. Operational Prediction Curves for Oxygen Gas in the Cryogenic Target Chamber	100
22. Observation of the $O^{18}(p,n)$ Yield at 2.642 MeV	104
23. Observation of the $O^{18}(p,n)$ Yield at 2.642 MeV	107
24. $O^{18}(p,n)$ Yield as a Function of Input Gas Flow	109
25. $\Delta E_n / \Delta E_p$ for $O^{18}(p,n)$ at $\Theta = 20^\circ$ and $160^\circ$	113
26. $O^{18}(p,n)$ Neutron Energy Resolution, $\Theta = 20^\circ$	115
27. $O^{18}(p,n)$ Neutron Energy Resolution, $\Theta = 160^\circ$	117



## LIST OF TABLES

1. Observed Resonances in $O^{18}(p,n)F^{18}$	48
2. Neutron Energy Resolution, $\Theta = 20^\circ$	66
3. Neutron Energy Resolution, $\Theta = 160^\circ$	74



A HIGH RESOLUTION STUDY OF THE  $\text{O}^{18}(\text{p}, \text{n})\text{F}^{18}$  REACTION



## CHAPTER I

### INTRODUCTION

The  $\text{Li}^7(\text{p},\text{n})\text{Be}^7$  reaction is commonly used as a source of neutrons for resonance studies of total neutron cross sections in the keV region. It is generally believed by researchers in the field that the ultimate neutron energy resolution is not instrumental but is limited by the thickness and uniformity of the lithium metal film. From the point of view of neutron yield, thin lithium targets can be made, but this average thickness is always less than the minimum average proton energy loss of around 600 eV. This limit is probably due to a crystalline growth of the lithium on the target backing so that the substrata is not covered uniformly. It was for this reason that the development of a windowless gas target chamber was initiated several years ago.

With the  $\text{A}^{40}(\text{p},\text{n})\text{K}^{40}$  reaction, Parks (1963) demonstrated the feasibility of the cryogenic target chamber for producing thin uniform gas targets ( $\sim 100$  eV proton energy loss or about  $10^{16}$  atoms/cm<sup>2</sup>). Targets can





easily be made thinner but the effect cannot be observed experimentally because of the incident beam spread, Doppler spread, and the natural width of the (p,n) resonances. Also a practical limit on the thinness of a target serving as a neutron source is imposed by the necessity of obtaining a considerable neutron yield. The  $A^{40}(p,n)$  reaction was unsuitable as a neutron source because of the lack of yield between its narrow resonances.

Instead the use of tritium gas in the cryogenic target chamber for the production of monoenergetic neutrons from the  $T^3(p,n)He^3$  reaction has been considered (Parks et al., 1964). The kinematics of this reaction should allow excellent resolution for neutrons selected at  $160^\circ$  with respect to the incident proton beam by the Duke neutron collimator (Nichols, Bilpuch, and Newson, 1959). Furthermore, like  $Li^7(p,n)$ , this reaction has a continuous yield above threshold, but there is no low lying state in  $He^3$  to give rise to a second energy group of neutrons.

However, before going directly to tritium gas as a neutron source, several problems inherent with its use were investigated. First the radioactive nature and high cost of tritium require the limitation of a small quantity of gas (2 or 3 liters at NTP) that must be completely recovered from the target chamber after each run. Secondly, although the thickness of the target and the translational Doppler effect of the target atoms would have negligible effect on the neutron resolution, there was the possibility that the



zero point vibrational motion of the di-atomic tritium molecule would introduce an appreciable Doppler spread. Lastly the feasibility of using the cryogenic target chamber to make high resolution neutron transmission measurements remained to be demonstrated.

The  $O^{18}(p,n)F^{18}$  reaction appeared to be a good test case for an investigation of the above mentioned problems. The cost of this rare isotope of oxygen (0.204% abundant) warranted the development of a handling and recovery system for use in conjunction with the cryogenic target chamber. This system was designed for convenient adaptation to tritium as well as other rare gases. Previous investigations of the  $O^{18}(p,n)$  reaction indicated the presence of several large resonances that could furnish (over a narrow range) a sufficiently continuous yield of neutrons for transmission measurements (Hill and Blair, 1956). Resolution calculations for this reaction, including the vibrational Doppler effect of the  $O_2$  molecule, showed that a total neutron energy spread on the order of 200 eV at 30 keV could be expected. This is comparable to the expected, but never realized, resolution of back angle neutrons from the  $Li^7(p,n)$  reaction where experimental observations have been consistently greater by a factor of two.

In addition to using the  $O^{18}(p,n)$  reaction as a trial gas target neutron source, it was decided to take advantage of the existing experimental apparatus to make a high resolution study of the relative total yield of this reaction from threshold to several hundred keV neutron energy. A precision



Q-value for the reaction was also obtained from the simultaneous measurement of a neutron and proton energy near threshold through a method involving the transmission technique of neutron spectroscopy.



## CHAPTER II

### APPARATUS

The windowless cryogenic gas target chamber has been described previously (Parks, et al., 1964) and is shown in Figures 1 and 2. The procedure for determining in advance how oxygen gas would be used in this target chamber is given in Appendix B along with experimental data indicating how the target density may be controlled. The data also proves the success of our method of predicting the operating characteristics of a target gas.

The necessity for calculating in advance the behavior of each gas used in the cryogenic target chamber may be seen by examining the role played by the temperature gradient rod. As shown in Figure 2 this rod serves to maintain a temperature gradient between the main refrigerant container and the inner chamber consisting of the reaction tubes and cooling cavity. The approximate equation governing the flow of heat through the gradient rod to the main refrigerant is

$$H = \frac{\bar{KA}}{L} (T - T_f) \quad \text{watts,} \quad (1)$$

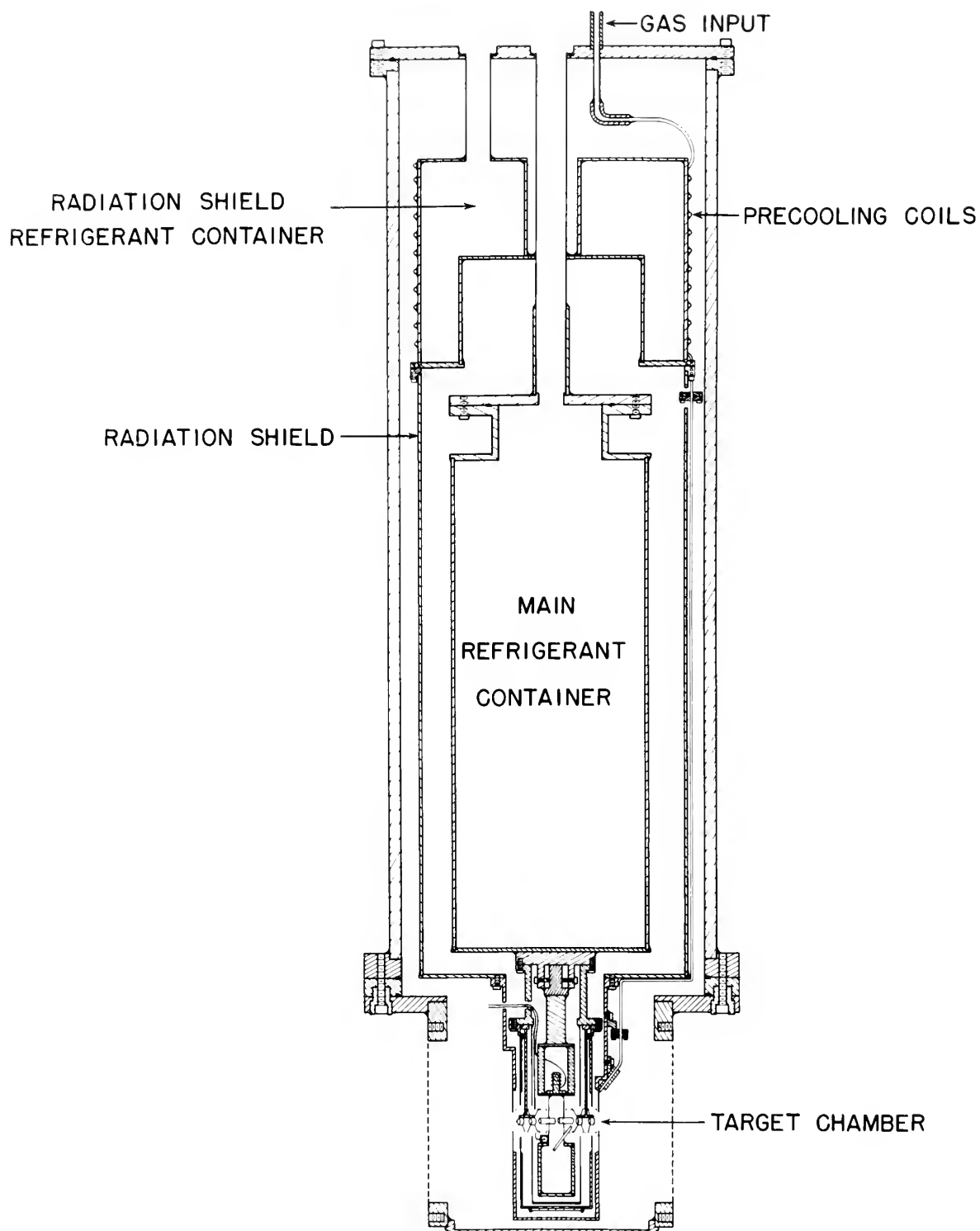
(6)







Figure 1. Cryogenic Gas Target System

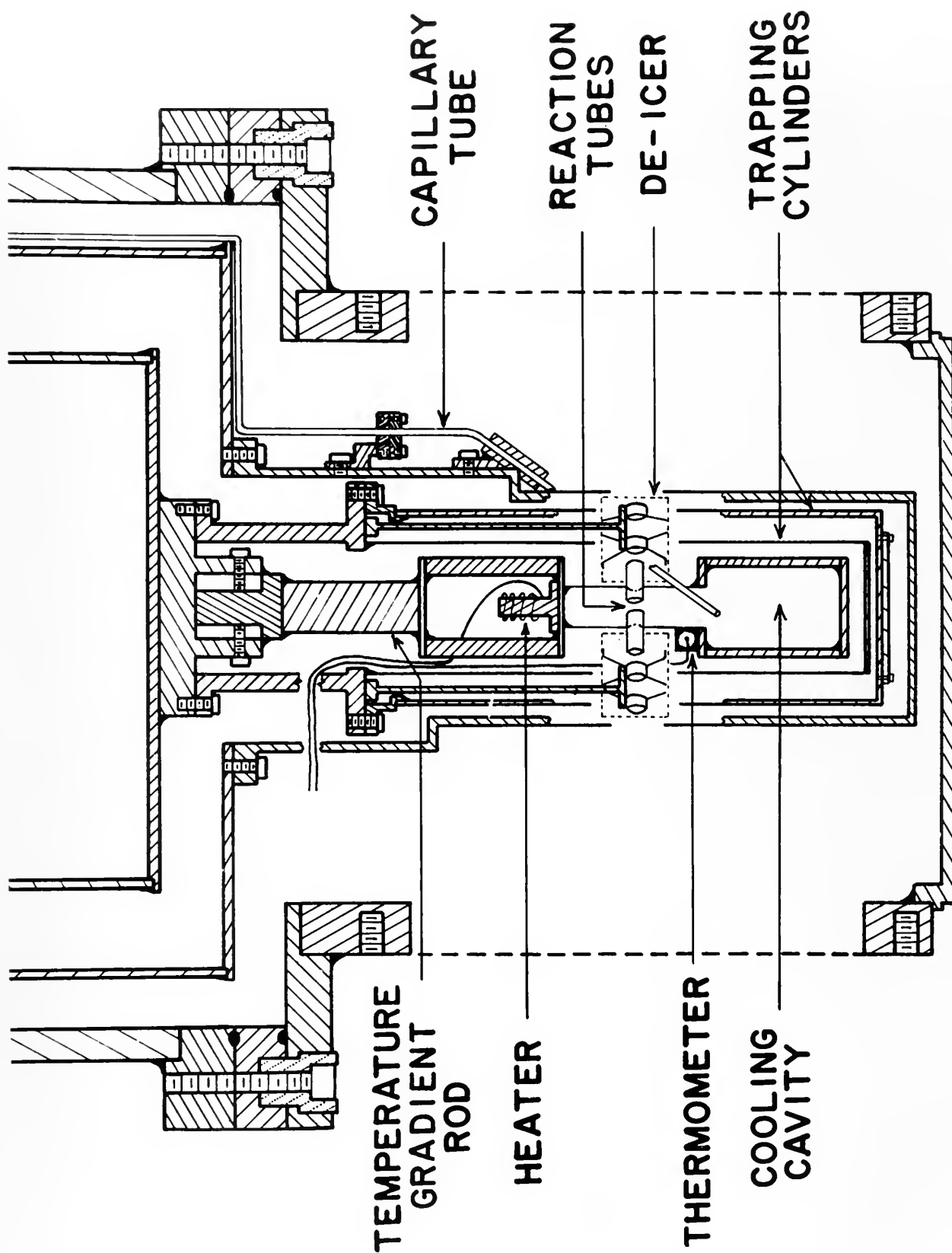


**CRYOGENIC GAS TARGET**





Figure 2. Cryogenic Target Chamber  
(Enlarged View)







where  $A$  = cross sectional area and  $L$  = length of the gradient rod,  $T$  = inner chamber temperature,  $T_f$  = main refrigerant temperature, and  $\bar{K}$  = average conductivity of the gradient rod over the temperature range  $T$  to  $T_f$ . The two important sources of heat applied to the inner chamber are that due to the input gas flow, and the electrical energy supplied to the target heater which consisted of a wire-wound resistor. (Fig. 2)

The inner chamber must be operated at a temperature high enough to prevent condensation of the input gas within it. As pointed out in Appendix B the maximum target density for a given gas flow occurs when the escape rate of the gas from the reaction tubes (just above the condensation temperature) is equal to the input rate. If condensation were allowed to take place within the inner chamber, the eventual result would be a thick solid target or the blockage of the input capillary tube in the cooling cavity. (Fig. 2) In the meantime the target gas density achieved would be considerably lower than optimum.

Therefore as seen from Eq. (1) the temperature gradient rod plays a very important part in the determination of the operating temperature. It must also allow the attainment of this temperature without an excessive heat input to the main refrigerant. At the same time we must be able to use gas flows large enough to give sufficient target density without raising the operating temperature to the point where convective heating of the trapping cylinders becomes serious. Since there are appreciable differences between



the specific heats of various target gases, the factor  $\bar{KA}/L$  of the gradient rod may have to be adjusted for a particular gas in order to achieve a satisfactory solution to our operating requirements. Considerable experimental time and effort can be saved by anticipating the behavior of each gas to be used in the cryogenic target chamber.

As both tritium and  $O^{18}$  gas are quite expensive and since tritium poses a definite health hazard, a system was developed for recovery of these gases after being fed into the cryogenic target chamber. This system had to satisfy the following requirements: (1) be able to recover the gas used in an experimental run with a minimum of loss or contamination; (2) be able, after recovery, to resupply the gas at a constant rate to the cryogenic target chamber; (3) be adaptable for use with both  $O^{18}$  and tritium as well as other gases; (4) be built in such a manner as to minimize the possibility of escape of tritium to the outside; and (5) be easily portable and of appropriate size to fit into available laboratory space.

The basic ideas for the gas recovery system were derived from a Chalk River experiment involving the acceleration of tritium ions (Allen and Almquist, 1953). A detailed account of the construction and operation of the rare gas handling and recovery system appears in Appendix A while the main points will be covered here.

Aside from the liquid helium trap and automatic safety valve which will be described later, all parts of the system are contained in a mobile



table--see Fig. 3. This gave the necessary flexibility since the cryogenic target chamber had to be moved three times during the experiment.

Equipment on the table consists of two mercury diffusion pumps, one oil diffusion pump, two cold traps, a manual piston pump, two gas reservoirs, a backing pressure gauge, and associated valves and plumbing. Each of the pumps has its own vapor baffle and trap.

The first mercury diffusion pump--see schematic diagram, Fig. 19, page 84 --is backed up by the second one which has a very high backing pressure tolerance. The cold traps serve to catch contaminants such as oil and water vapor. The manual piston pump is used for maintaining the necessary backing pressure and for recovering the last traces of the target gas after a run. The two gas reservoirs are essentially cold traps to condense and store the recovered gas. During a run one serves to supply the gas and the other to recover it from the target chamber after a run is concluded. The oil diffusion pump maintains a separate vacuum for thermal insulation of the gas reservoirs. The input gas flow to the target chamber is regulated with a needle valve and monitored with a flow-rate meter--see Appendix A.

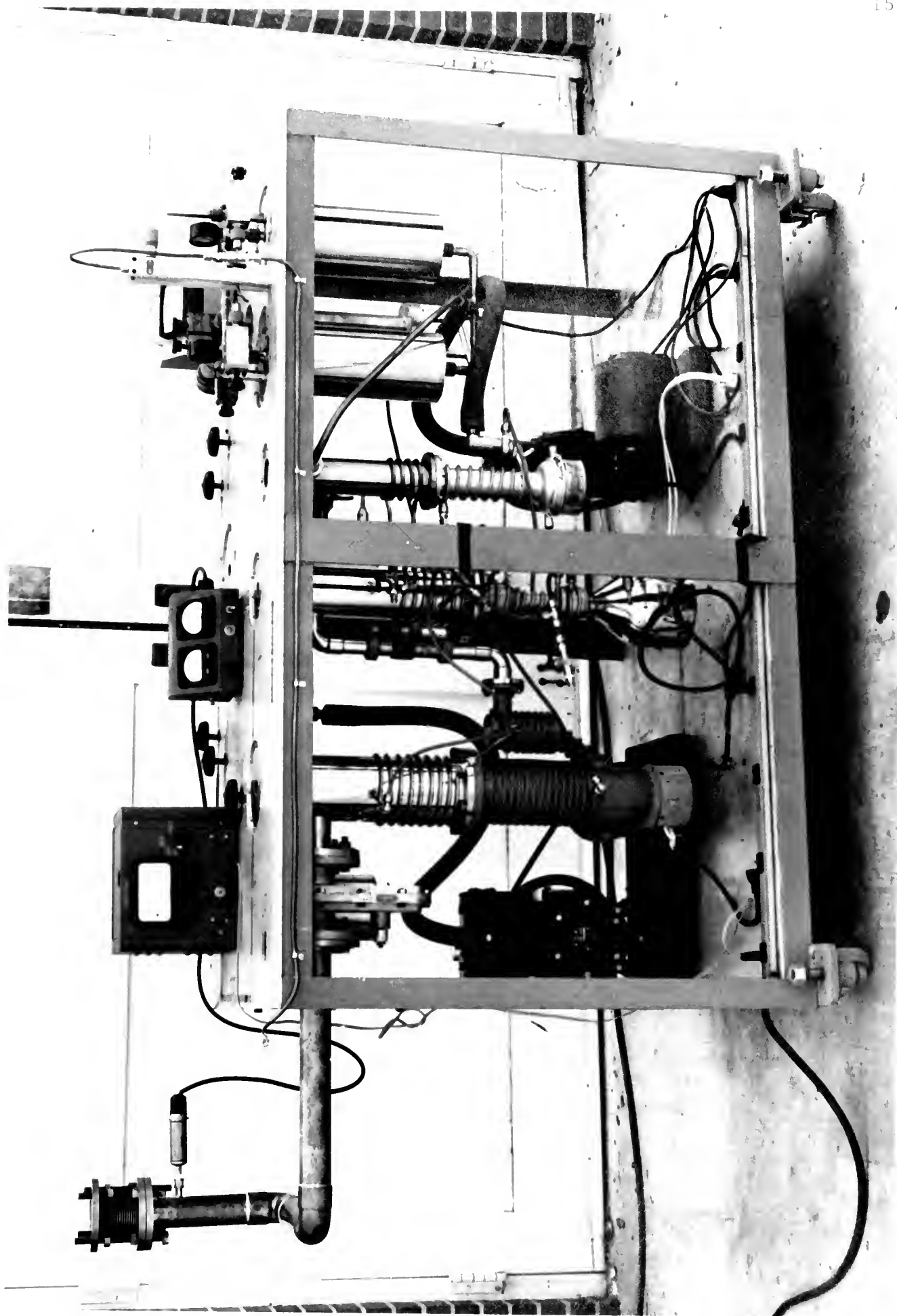
A liquid helium trap is placed directly in the beam path and serves to catch the small amount of target gas that escapes past the opening to the first diffusion pump of the recovery system and passes up the beam pipe toward the accelerator. It is based on a design suggested by





Figure 3. Rare Gas Handling and Recovery  
System Table







Parks (1964) and shown in Fig. 4. The radiation baffle shields the trapping cylinders from virtually all room temperature radiation. It is maintained, of course, at liquid nitrogen temperature ( $77^{\circ}\text{K}$ ) and has a carbon coating on the inside surfaces to prevent reflection. It was found that with this precaution one liter of liquid helium would boil away in 42 hours or more; otherwise the lifetime was around six hours. The beam hole through the center was left large enough to allow for shrinking of the trap when cooled.

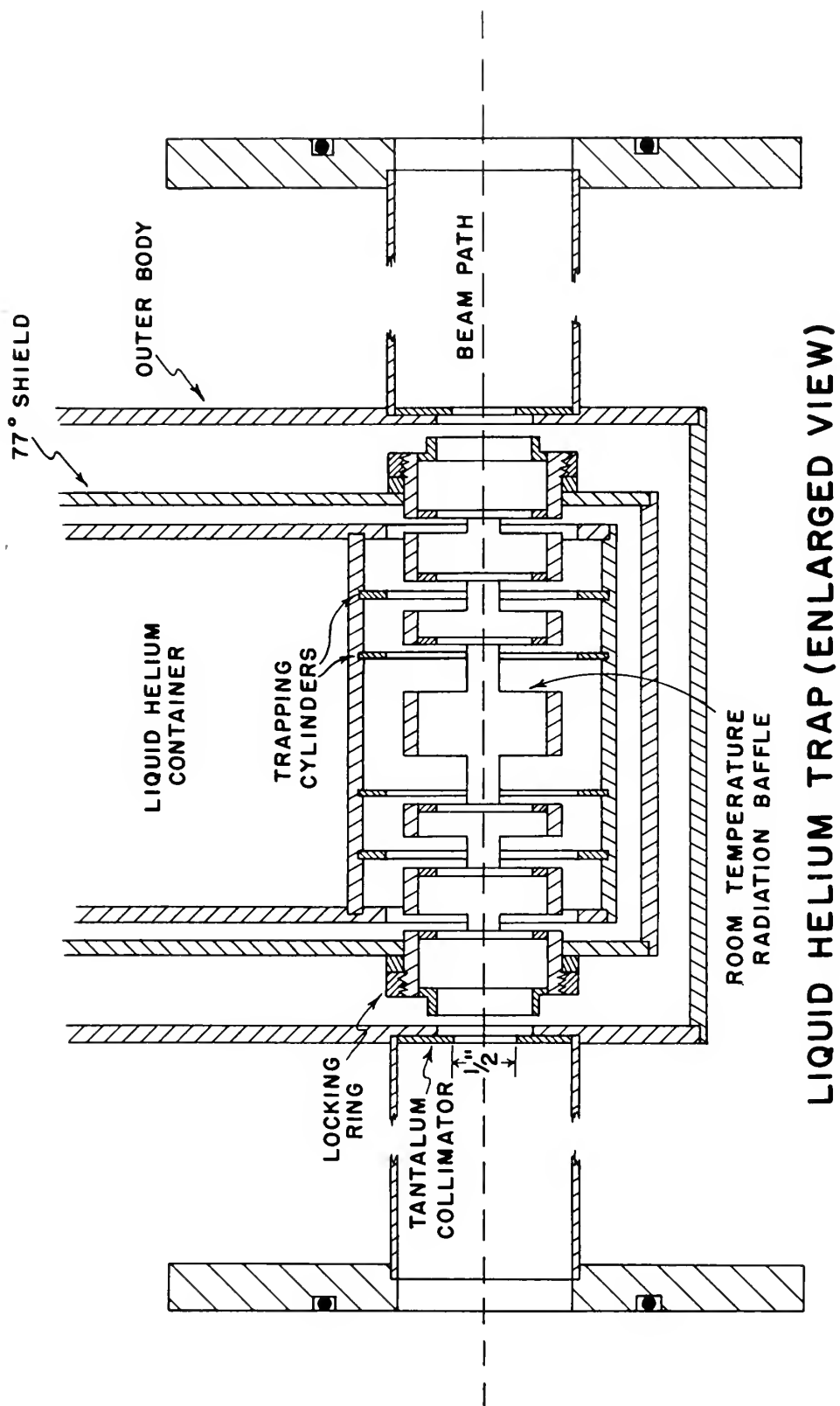
The amount of oxygen gas lost during the entire experiment was only 0.125% per cycle. This trapping action should prove of considerable importance in minimizing the contamination of the accelerator and cylindrical analyzer when tritium gas is used. For some gases liquid nitrogen can be used in both this trap and as the main coolant in the cryogenic target itself.

An electro-pneumatically operated VRC one inch gate valve with a closing time of less than  $1/5$  sec. was placed on the accelerator side of the liquid helium trap. This valve serves as an automatic safety device against an accidental release of a large quantity of target gas into the vacuum system. For example, if the liquid helium used with the cryogenic target chamber were to boil away prematurely, there would be a rapid release of condensed gas as the trapping cylinders warmed up. The liquid helium trap would be unable to condense such a concentration





Figure 4. Liquid Helium Trap  
(Enlarged View)







of gas, and a considerable amount would be lost up the beam pipe before any valve could be closed manually. This behavior has been observed with deuterium, argon,  $\text{BF}_3$  and other gases.

The valve is closed automatically when the ionization current from a Philips vacuum gauge becomes high enough. For this experiment the valve was set to operate at a pressure of  $8 \times 10^{-4}$  torr. The valve may also be actuated manually with push buttons from the Van de Graaff console or from the experimental area. It has the added feature of closing when there is a power failure.

Whenever the valve closes, a beam stop is actuated which cannot be removed until the valve is opened. This provision protects the valve seat from being accidentally overheated by the proton beam.



### CHAPTER III

#### EXPERIMENTAL CONDITIONS AND PROCEDURE

This experiment was carried out in two phases. The first consisted of measuring the relative total yield of the  $O^{18}(p,n)F^{18}$  reaction. The second involved using this reaction as a neutron source and taking transmission measurements on various samples in order to determine the actual neutron energy resolution attainable with the cryogenic target chamber. Experimental conditions applicable to both phases will be described first.

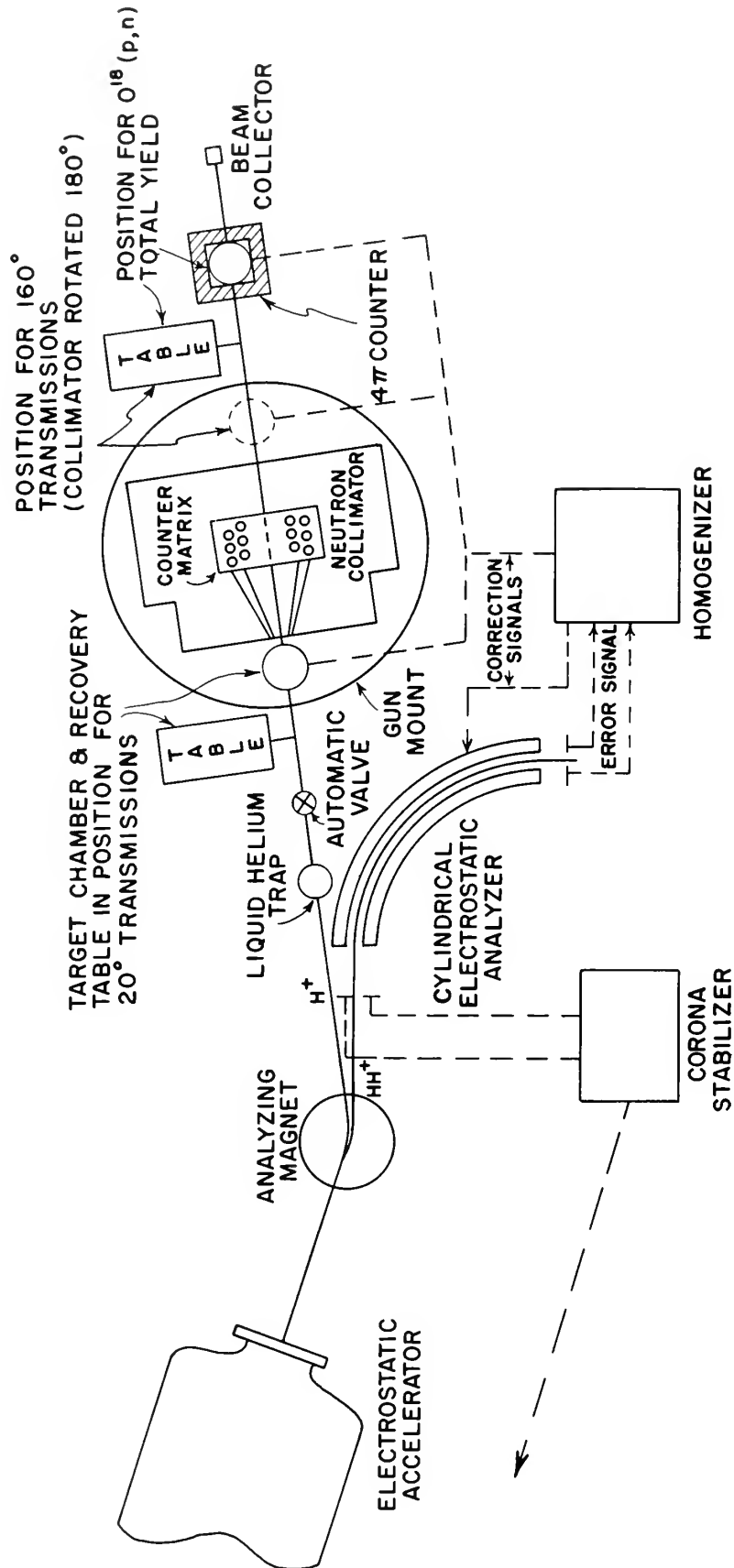
##### A. Total Yield Measurement

Referring to the schematic floor plan of Figure 5, protons were accelerated with the Duke 3 MeV Van de Graaff. The time fluctuation of the energy of the proton beam was largely eliminated by use of the homogenizer (Parks, Newson, and Williamson, 1958); the  $HH^+$  beam, in passing through a one meter cylindrical electrostatic analyzer, generates





Figure 5. Experimental Floor Plan



EXPERIMENTAL FLOOR PLAN





a compensating voltage which is applied to the cryogenic target chamber. Proton energies were determined with the cylindrical analyzer calibrated against the  $\text{Li}^7(p,n)\text{Be}^7$  threshold which was taken to be  $1880.7 \pm 0.4$  keV (Marion, 1961). With the homogenizer, proton energy steps as small as 50 eV could be taken (Parks et al., 1964). A  $\text{Li}^7(p,n)$  threshold calibration was taken at the beginning and at the completion of each experiment.

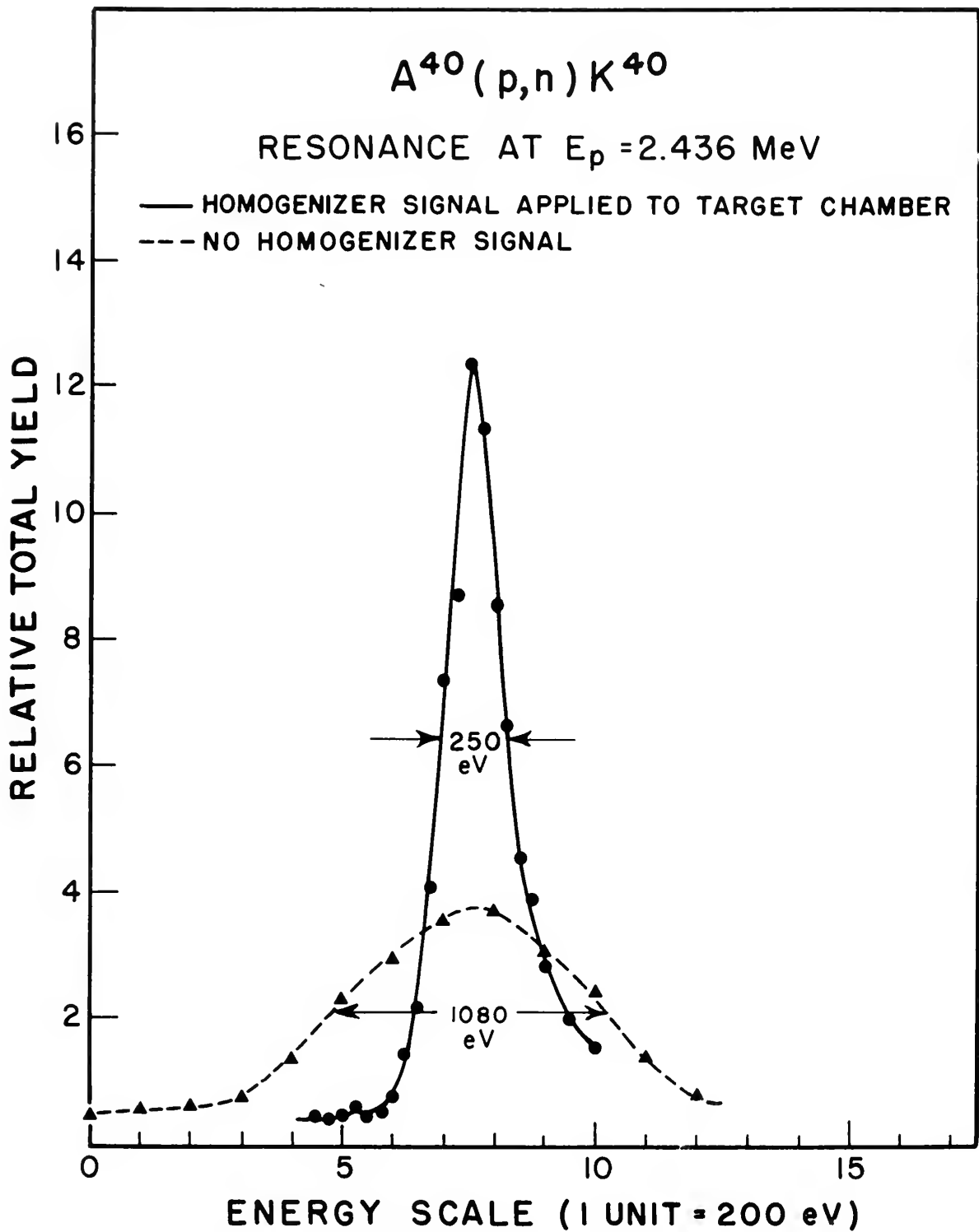
From a thick target measurement of the  $\text{C}^{13}(p,\gamma)\text{N}^{14}$  resonance, Kyker and Williamson (1962) found that the effective proton spread after analysis was about 400 eV at 1.746 MeV. This represents a resolution of about 1/4000 without use of the homogenizer. Unfortunately during the course of the experiment there was a deterioration in uncorrected beam resolution. The narrow  $\text{A}^{40}(p,n)\text{K}^{40}$  resonance at 2.436 MeV (Parks, 1963) was observed with the cryogenic target chamber. From Figure 6 it is seen that the uncorrected beam spread is on the order of 1 keV which indicates a resolution of 1/2500. With homogenizer voltage applied to the target chamber the beam spread was reduced to around 220 eV (1/11000). (This value is obtained from the observed width of 250 eV after allowing for the effects of Doppler broadening and the estimated natural width of the resonance.) The observed width of this peak at half maximum had previously been found to be 190 eV with the homogenizer.

The exact reason for the deterioration of the beam resolution was not determined during the course of the experiment. Considerable difficulty





Figure 6.  $A^{40}(p,n)$  Resonance at 2.436 MeV.  
Indicates effective proton energy spread  
after homogenizer correction.





was experienced with the Van de Graaff source electronics during this time and the overall stability of the machine was below standard. This fact along with an aging accelerator tube (more than 3600 hours running time) probably accounts for the 1 keV spread. Little success was had in reducing this width by adjusting the focusing properties of the beam analyzing magnet or varying the position of the  $\text{HH}^+$  beam at the object slits of the cylindrical analyzer. Therefore, for purposes of neutron resolution calculations, a corrected proton energy spread of 1/11000 has been used as measured above.

At the beginning of the experiment the cryogenic target chamber and the recovery and handling system table were placed in the position for total yield work --see Figure 5, page 22. In this position the neutron collimator water tank acts as a shield for the target chamber against neutrons produced by the beam on the other side of the tank.

The available target gas consisted of one liter (NTP) of oxygen enriched to 65%  $\text{O}^{18}$  which was purchased from the Isomet Corporation, Palisades Park, N.J. at a cost of \$1600. Before introducing the gas into a reservoir on the table, the operation of the entire system was tested using natural oxygen. This included checking the reliability of the automatic safety valve circuit, the performance of the liquid helium trap, (where the necessity of the room temperature radiation baffle was found), checking for leaks, and testing the capability of the table for recovering





the gas and then supplying it again to the target chamber at a constant rate. Most of the procedures for operating the system were worked out at this time.

The target gas was supplied in a Pyrex bulb fitted with a break-seal. A rubber vacuum hose was connected between the neck of the bulb and the input to a gas reservoir; this volume was evacuated to a pressure of less than  $10^{-4}$  torr. The outer jacket of the reservoir was filled with liquid nitrogen and evacuated in order to reach a temperature of about  $56^{\circ}$  K. Next the breakseal was opened allowing the oxygen to liquify in the reservoir which was then sealed off with a valve. It was estimated that only 0.23% of the gas was lost in transfer.

In measuring the yield of the  $O^{18}(p,n)F^{18}$  reaction, it was decided to cover a range from several keV below reported threshold at 2.577 MeV (Hill and Blair, 1956) to as high an energy as practicable with the 3 MeV Van de Graaff machine. To prevent heating of the reaction tubes the incident proton beam was sharply defined with an adjustable water cooled collimator (Parks, 1963). Alignment of the target chamber and collimator was accomplished visually with a telescope mounted beyond the beam collector. The end piece of the collector housing is clear lucite; the collector cup can be raised to allow viewing. The neutrons were detected in an unshielded  $BF_3$  counter matrix surrounding the cryogenic target chamber which subtended a solid angle of approximately  $0.93(4 \pi)$  steradians.



Since only one liter of oxygen gas was available, the input gas flow was adjusted to 5 cc/min. This gave about  $2\frac{1}{2}$  hours in which to take data before recovery of the gas for the next run. A preliminary measurement of the reported peak in the excitation curve at 2.657 MeV (Mark and Goodman, 1956) was made using natural oxygen (0.204 percent  $O^{18}$ ). The data indicated that 5 cc/min. would give sufficient yield.

Since the  $BF_3$  counter matrix was unshielded except for the shadow effect of the water tank mentioned earlier, the main problem in measuring the  $O^{18}(p,n)$  yield was a high background rate. Most of this background was produced from protons striking the collimator apertures directly before the target chamber. It was found that the tantalum diaphragms absorbed  $O^{18}$  when exposed to the relatively rich atmosphere of oxygen gas during the recovery cycle. The rate of  $O^{18}$  build-up was directly proportional to the number of exposure periods. Thus, before each run, the tantalum pieces had to be thoroughly cleaned in order to maintain a relatively reproducible background rate. In addition, at energies above 3 MeV, there was a considerable  $Cu^{65}(p,n)$  background from scattered protons.

While measuring the yield curve 1/2 keV proton energy steps were taken from 2.565 to 2.790 MeV and 1 keV steps thereafter. With an average beam of  $2.5\ \mu A$  through the target chamber, counting times were only 4 sec. for each point. Closer steps were taken over two regions



where small resonances appeared. The relative efficiency of the detection system was checked before each run by placing a neutron source at a fixed distance from the counter matrix. A background curve was taken at the end of each run after turning off the gas flow and allowing the target chamber to reach static equilibrium. The results of the total yield work are discussed in Chapter IV.

### B. Transmission Measurements

The recovery system table and cryogenic target chamber were moved in front of the neutron collimator tank which was rotated to the  $20^\circ$  position as shown in Figure 5, page 22. The design and operation of the Duke neutron collimator and associated detection system has been reported by Nichols, et al., (1959); the cryogenic target chamber was designed for use with this neutron collimator. Neutrons at  $20^\circ$  from the axis of the incident proton beam have only to pass through several mils of silver and one meter of air in passing from the target chamber to the detector.

The angular opening of the  $20^\circ$  neutron collimator leading to the counters may be varied between  $0^\circ$  and  $2^\circ$ . A  $60^\circ$  arc at both the top and bottom of the opening of the neutron collimator is blocked off to neutrons and the counters are arranged in two separate groups giving a left bank and a right bank (Nichols, et al., 1959). The samples in



which transmissions are taken have to be placed between the target chamber and the face of the collimator in order to "shadow" each bank. Samples are made in the form of semicircular rings of constant thickness and shadow each bank of counters alternately while the other bank serves as a monitor. At each neutron energy both a left bank and right bank transmission are taken for a preset monitor count. These are then averaged to cancel differences in the efficiency or geometry of the banks.

The target chamber must be accurately positioned so that the center of the reaction tubes lies at the apex of the acceptance cone of the neutron collimator as shown in Figure 7. In addition the incident beam must be accurately aligned with the axis of the neutron collimator cone; otherwise, due to the different angles involved, there would be an average energy difference between the neutrons seen by each counter bank. The cone axis was defined by placing a tube with cross hairs inside the beam pipe opening along the axis of the cone. The proton collimator apertures and reaction tubes were then adjusted to lie along this axis with the aid of the telescope.

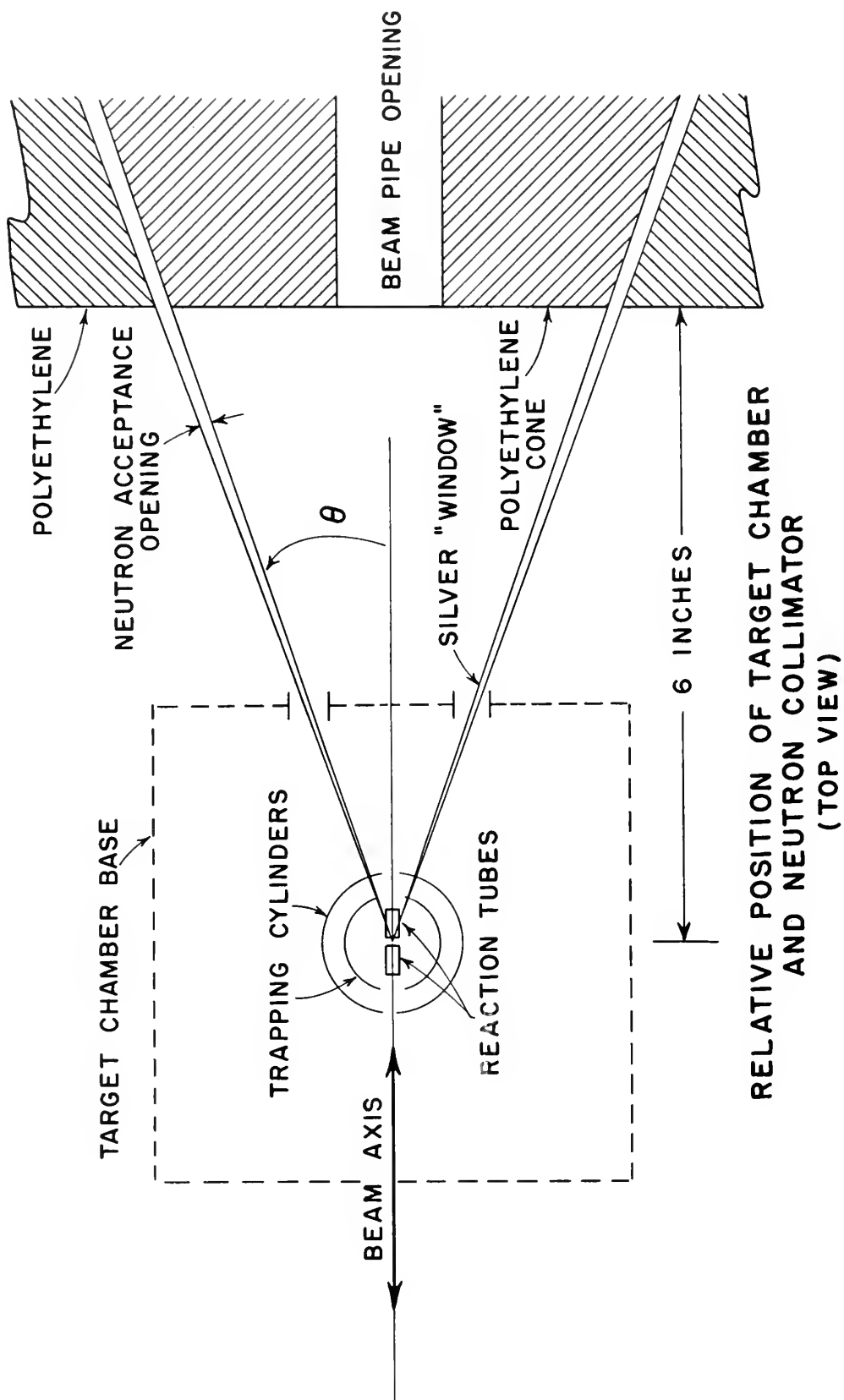
From the total yield work of the  $O^{18}(p,n)F^{18}$  reaction only two regions were found where the intensity of keV neutrons would be sufficient for transmission measurements--see Figures 9 and 10, Chapter IV. The resonance at 2.643 MeV proton energy gave a useful neutron energy range from 102 to 114 keV while that at 3.025 MeV gave a range of 505







Figure 7. Relative Position of Target Chamber  
and Neutron Collimator





to 545 keV. Although resonances above this energy could have been used for taking other transmissions, there was no particular interest in checking the neutron resolution above 550 keV.

Because of the narrow neutron ranges available and high resolution expected, it was very important to obtain a good Q-value for the reaction in order to predict neutron energies accurately. Starting with a rough Q-value estimated by subtraction of tabulated masses, a corrected value was determined by observing known neutron total cross section resonances at 98 keV in fluorine and at 105.5 and 110 keV in natural strontium. This method is discussed in Chapter IV; neutron resonances in natural potassium were also measured in the lower energy region. A sample of natural iron was used to check neutron resolution at the higher energies (510-535 keV).

Due to the thin gas target ( $< 100$  eV) and relative low yield of the  $O^{18}(p,n)$  reaction at the energies involved, transmission points were taken with a monitor or "sample out-count" of 1000 or 2000 instead of the customary 5000 "out-count". The angular opening of the neutron collimator was varied between  $0.25^\circ$  to  $1.0^\circ$  to check this effect on neutron resolution, but most of the data was taken with an opening of  $0.5^\circ$ . With 15 to 20  $\mu$  A of protons passing through the target chamber and a  $0.5^\circ$  opening, counting times for 1000 out-count ranged from 0.25 min. on the peaks of the  $(p,n)$  resonances to 1.5 min. on the tails. As a



compromise between higher target densities (see Appendix B) and available gas supply, a 10 cc/min. gas flow was used which gave a running time of approximately  $1 \frac{1}{4}$  hours for each gas cycle. This allowed the measurements to cover 6-10 keV during a run taking 1/8 keV steps in neutron energy.

Although the neutron collimator system effectively shielded the counter banks from neutrons produced at the beam defining apertures, an additional background source was found. The 30 mil thick disc of tantalum at the rear of the beam collector cup had become contaminated with  $O^{18}$ . Hence there was a strong source of background neutrons located at a point where a single scatter could send them up the angular opening of the collimator. To avoid having to clean the tantalum disc before each run it was replaced with a 20 mil disc of platinum which proved to be resistant to oxygen contamination. As a further precaution the main defining aperture of the proton collimator was replaced with one of platinum. The background from the beam collector cup was not noticed during the total yield work since apparently it was small in comparison with that from the proton collimator.

In spite of the partial success with platinum, the residual background level was high enough to account for 10% of the total counts on points taken with the low yield tail of a (p,n) resonance.

In the final step of the experiment the neutron collimator tank was





rotated  $180^\circ$  and the cryogenic target chamber was moved to the position for  $160^\circ$  transmission measurements--see Figure 5, page 22. At this angle (with respect to the incident beam) better neutron resolution than at  $20^\circ$  may be obtained below 300 keV. This is due mainly to more favorable ratios of  $\Delta E_n / \Delta E_p$  and  $\Delta E_n / \Delta \Theta$  where  $\Delta \Theta$  is the angular opening of the neutron collimator.

However taking data at  $160^\circ$  presented several new problems. The apex of the neutron collimator acceptance cone lies only six inches out from the face of the collimator tank. Hence, with the target chamber in proper position, there was no space for the regular proton collimation system. In order to minimize the possibility of scattered beam striking the reaction tubes, the defining apertures must be placed immediately before the target chamber. Therefore a new proton collimation system was designed to fit inside the one inch O.D. beam pipe that passes through the center of the neutron collimator cone. As shown in Figure 8 this collimator is not water cooled but was made of thick brass to allow for heat dissipation by thermal contact with the beam tube. Because of the observed heating effect of the proton beam, any future design of this collimator will incorporate water cooling. The position of this proton collimator was fixed so that the beam, in passing through it, was automatically aligned with the axis of the neutron collimator cone. The target chamber could then be adjusted visually with the telescope in



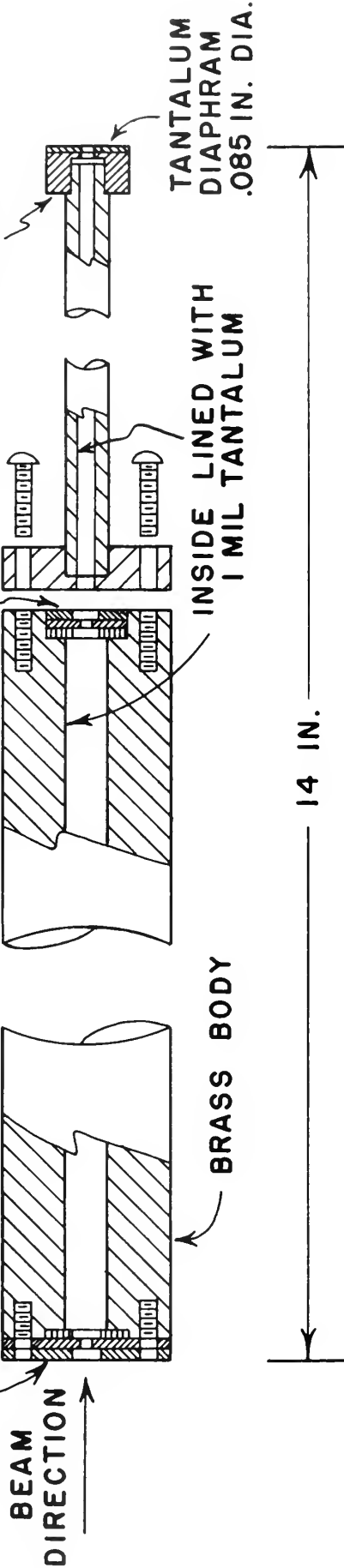


Figure 8. Proton Collimator Assembly (160° Work)

30 MIL TANTALUM DIAPHRAMS  
HOLE DIA.  $\frac{1}{8}$ ,  $\frac{1}{16}$ ,  $\frac{1}{8}$  IN.  
FROM LEFT TO RIGHT

FIRST AND LAST DIAPHRAM-TANTALUM  
CENTER-20 MIL PLATINUM  
HOLE DIA.  $\frac{1}{8}$ , .065,  $\frac{1}{8}$  IN.

SOAPSTONE  
INSULATOR



## PROTON COLLIMATOR ASSEMBLY (160° WORK)



order to place the reaction tubes along this axis. The remainder of the beam pipe passing through the detectors and neutron collimator was carefully lined on the inside with cadmium sheet to prevent neutron production by protons scattered from the first beam defining aperture. The  $\text{BF}_3$  counters are particularly vulnerable to background neutrons produced in this vicinity.

At  $160^\circ$  the smaller  $\Delta E_n/\Delta E_p$  ratio also means that the effective neutron energy range for taking transmission data was reduced relative to that available with the  $20^\circ$  collimator. The effective neutron range from the  $\text{O}^{18}(\text{p},\text{n})$  resonance at 2.643 MeV was only 26 to 30 keV and that from the 3.025 MeV resonance, 290 to 307 keV, but the latter range was not of much interest.

The anisotropic yield of the  $\text{O}^{18}(\text{p},\text{n})$  resonances led to longer counting times for the  $160^\circ$  work compared to that at  $20^\circ$ . The yield of the 3.025 and 2.643 MeV resonances were down by factors of two to three. This meant that only about a 1 or 2 keV neutron energy range could be covered in  $1/8$  to  $1/16$  keV steps during a run over the 2.643 MeV region. With a predicted neutron energy resolution of 200 eV it was found necessary at times to take 60 eV steps. The longer counting times also resulted in a larger background to signal ratio.

In view of the limited energy range available the choice of narrow known neutron resonances was quite meager. Transmissions were taken





in samples of natural copper, yttrium, and natural cobalt at the lower energy region while samples of natural calcium and sodium were used at the 3.025 MeV region. However the results of the transmission measurements in this latter region were not conclusive enough to be included in the discussion of Chapter IV.



## CHAPTER IV

### DISCUSSION OF RESULTS

#### A. $O^{18}(p,n)F^{18}$ Cross Section

The  $O^{18}(p,n)F^{18}$  relative total yield measurements are shown in Figures 9, 10, and 11. The total proton energy span of 2.565 to 3.290 MeV was covered in three runs starting from the lower energy. Although the same input gas flow of 5 cc/min. was used in each run and the relative efficiency of the detection system was checked at the beginning of each run (Chapter III), the results of the last two runs had to be normalized to the first run by observing the yield at the peak of the resonance at 2.643 MeV. It was found that by using the same input gas flow as read from the Flo-gage (Appendix A) the target density could only be reproduced within  $\pm 10\%$  from day to day. On the last run where the region from 3.080 to 3.290 MeV was covered, considerable difficulty was experienced with the stability of the Van de Graaff accelerator. This is reflected in point scatter of the data of Figure 11. However,





Figure 9.  $O^{18}(p,n)F^{18}$  Relative Total Yield. To convert counts/10 micro-coulombs (above background) to millibarns, multiply by  $5.74 \times 10^{-3}$  (normalized to data of Blair and Leigh, 1960).

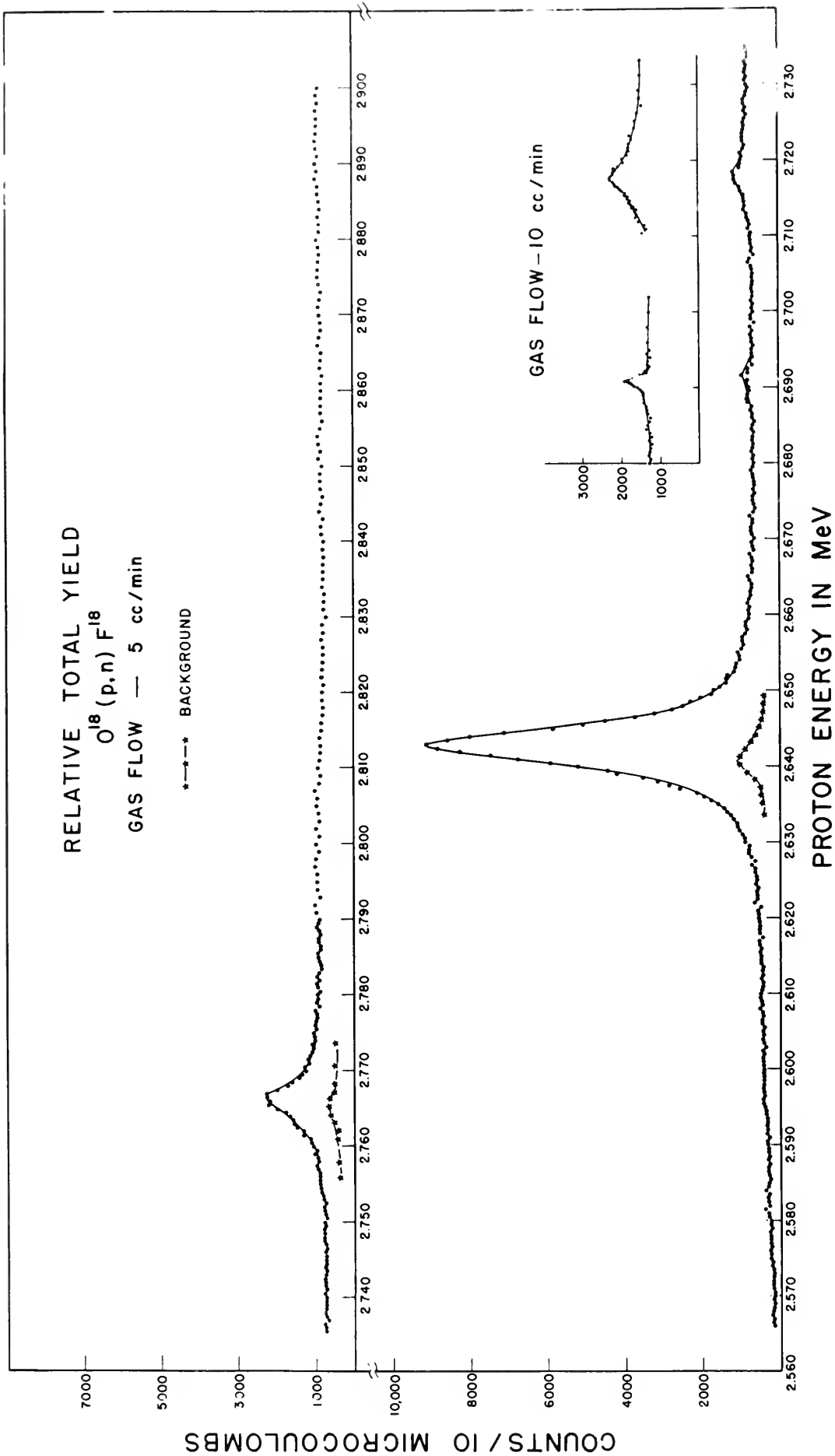








Figure 10.  $\text{O}^{18}(\text{p},\text{n})\text{F}^{18}$  Relative Total Yield. To convert counts/10 micro-coulombs (above background) to millibarns, multiply by  $5.74 \times 10^{-3}$  (normalized to data of Blair and Leigh, 1960).

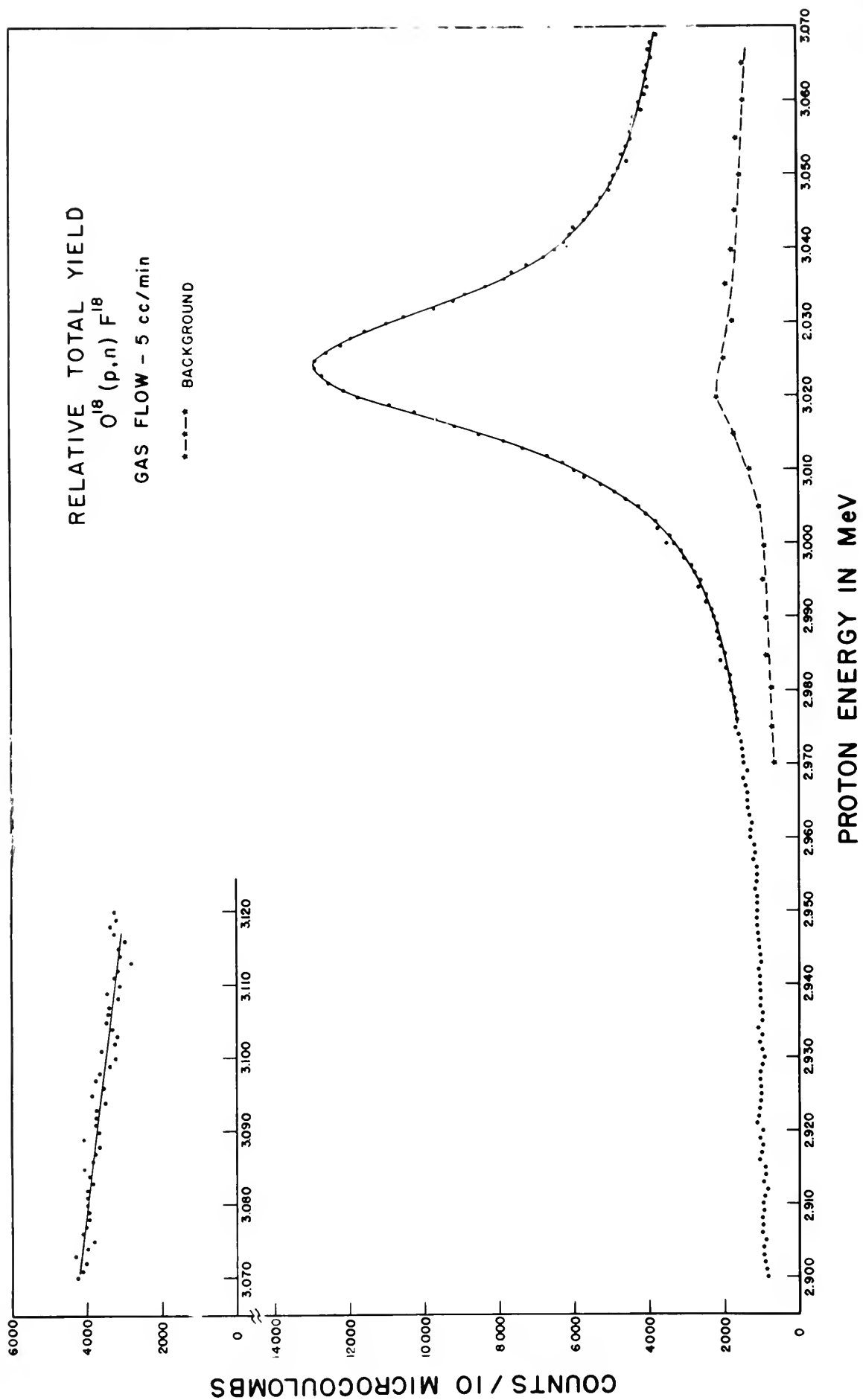






Figure 11.  $\text{O}^{18}(\text{p},\text{n})\text{F}^{18}$  Relative Total Yield. To convert counts / 10 micro-coulombs (above background) to millibarns, multiply by  $5.74 \times 10^{-3}$  (normalized to data of Blair and Leigh, 1960).

RELATIVE TOTAL YIELD

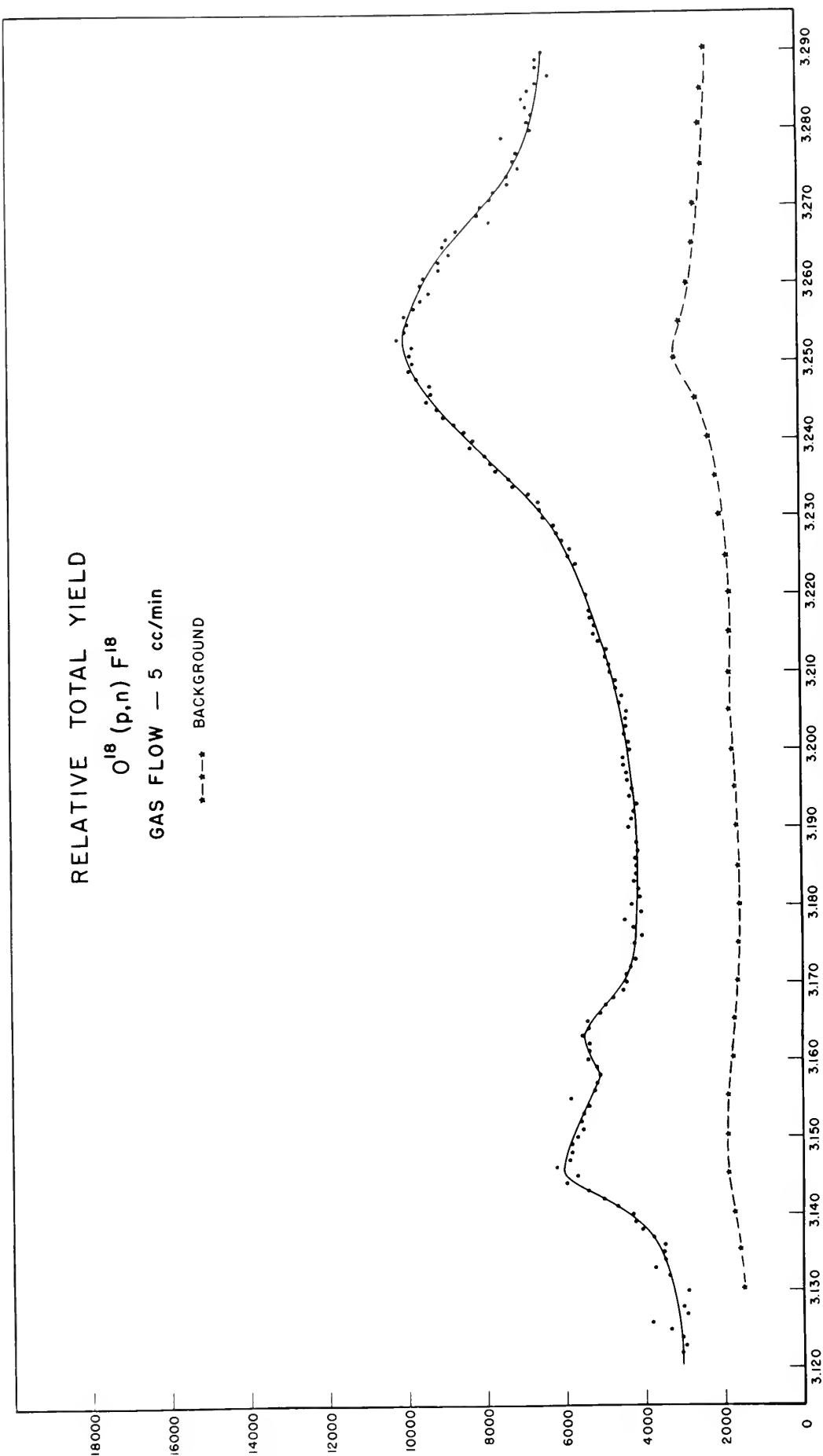
$O^{18} (p,n) F^{18}$

GAS FLOW — 5 cc/min

•-•-•- BACKGROUND

COUNTS / 10 MICROCOULOMBS

PROTON ENERGY IN MeV







it was decided not to repeat these measurements since the limit of the voltage capability of the 3 MeV machine was being approached.

The background shown beneath the data of each Figure was carefully measured at the end of a run as pointed out in Chapter III. The contamination of the proton collimator tantalum diaphragms is clearly evident from the background peaks which occur, on the average, 3.5 keV in proton energy below the true  $O^{18}(p,n)$  yield peaks. This difference corresponds to the average positive correction potential applied to the target chamber by the homogenizer. The steady rise in the residual background level is thought to be due to scattered protons striking brass around the target chamber and producing neutrons from the  $Cu^{65}(p,n)$  reaction. This reaction has a threshold at 2.169 MeV and a rapidly increasing yield above 2.7 MeV (Brugger, Bonner, and Marion, 1955).

A summary of the observed resonances corresponding to excited levels in the compound nucleus,  $F^{19}$ , is given in Table 1. The data is in essential agreement with that of Hill and Blair (1956) and Blair and Leigh (1960). However our negligible target thickness gave an effective proton energy resolution nearly two orders of magnitude better. For this reason a previously unreported level at 2.691 MeV proton energy was observed. This corresponds to an excitation energy of 10.541 MeV in  $F^{19}$ . As shown in the inset of Figure 9 a repeat run over this resonance



Table 1. Observed Resonances in  $O^{18}(p,n)F^{18}$

Resonance Number	Proton Energy	Width at Half Max.	Relative Peak Yield Above Background	Excitation Energy of Comp. Nucleus
1	$2643 \pm 1.0$ keV	$6.5 \pm 0.5$ keV	82	10.495 MeV
2	$2691 \pm 1.0$	$1.6 \pm 0.2$	5	10.541
3	$2717 \pm 1.0$	$5.5 \pm 0.5$	7	10.565
4	$2767 \pm 1.5$	$5.0 \pm 0.5$	16	10.613
5	$3025 \pm 2.0$	$26.0 \pm 1.5$	110	10.857
6	$3145 \pm 3.0$	12 (est.)	40	10.970
7	$3163 \pm 3.0$	11 (est.)	35	10.988
8	$3248 \pm 3.0$	$33.0 \pm 5.0$	73	11.068



and the small peak at 2.717 MeV was made with an increased target density in order to confirm their positions. In addition, the resonance reported at 3.163 MeV (Hill and Blair, 1956) was resolved into two peaks. Since each of our observed resonances is completely resolved, the energy values given for the yield maxima are considered correct to within the proton energy calibration error ( $\pm 1$  keV) plus the ability to distinguish the peak point from the data. These values differ by several keV from the earlier work where corrections for target thickness had to be applied. Also our observed widths at half-maximum are consistently less than the earlier values.

An absolute cross section for the  $O^{18}(p,n)F^{18}$  reaction is not given on Figures 9, 10, and 11 due to uncertainties in target density and the efficiency of the detector system. However, using a best estimate for target density of  $5 \times 10^{15}$  atoms/cm<sup>2</sup> (Appendix B) and an estimated 10% detector efficiency, the yield over the 2.643 MeV resonance was converted to cross section and an integrated comparison made with the data of Blair and Leigh (1960). This comparison indicated that our calculated cross sections were about a factor of two below their values which lies within their reported uncertainty of  $\pm 50\%$ . An improved technique for obtaining absolute cross section measurements for this reaction and others is planned for the near future.

Unfortunately the present design of the cryogenic target chamber



does not allow angular distributions of neutrons to be taken. Otherwise, with the excellent resolution available, the angular momentum of the excited levels in  $F^{19}$  could be determined from an analysis of such distributions. However, as pointed out in Chapter III, a marked anisotropy in the yields of resonances 1 and 5 between the lab angles of  $20^\circ$  and  $160^\circ$  was noted while using the  $O^{18}(p,n)$  reaction as a neutron source. This difference was much larger than could be accounted for by center of mass motion.

Since the ground state of  $O^{18}$  has spin  $I = 0^+$  (Lauritsen and Selove, 1959), only one channel spin,  $S = 1/2$ , has to be considered. Hence the anisotropic distributions of resonances 1 and 5 indicate that for these levels the quantum number  $J > 1/2$ . Mark and Goodman (1956) have measured the angular distribution of resonance 5 and placed a probable value for its spin of  $J = 3/2^+$ .

A direct observation of the yield near reaction threshold (Fig. 9) did not give a very accurate prediction for the threshold energy because of the thin target and resulting poor signal to background ratio in this region. Nevertheless the apparent intersection of the data and background curves gives a value in fair agreement with that determined by much more accurate means as described in Part B of this Chapter.





## B. Neutron Transmission Measurements at 20°

### 1. Q-Value Determination.

As pointed out in Chapter III an accurate determination of neutron energy was necessary since running times were too short to scan large regions in order to locate resonances previously measured by neutron transmission. Initially neutron energies were estimated from a Q-value obtained by subtraction of recent tabulated masses (Everling, et al., 1960). However, using a sample of teflon ( $C_2F_4$ ) for neutron transmission, the broad neutron resonance due to  $F^{19}$  near 100 keV was observed and it was found that the apparent neutron energy at the peak was about 10 keV higher than the reported value (Newson, et al., 1961a). This discrepancy indicated errors in the tabulated masses with the largest error probably occurring in that of the residual nucleus,  $F^{18}$ . This preliminary transmission data is not shown since it served only to give us a first order correction to the neutron energy.

Since, as stated previously, a good threshold value for the  $O^{18}(p,n)$  reaction could not be gotten from direct observation of the yield near threshold, an alternative method for obtaining an accurate Q-value had to be used. This method involves measuring a narrow neutron resonance where the neutron energy at the peak is known from previous experimentation. With our corresponding proton energies known relative to a  $Li^7(p,n)$



threshold calibration we can get a simultaneous determination of  $E_p$  and  $E_n$  at the peak of the resonance. Thus substitution of these two energies into the nonrelativistic Q equation (Evans, p. 411, 1955) yields a Q-value accurate to within the error of our proton energy calibration. The form of this equation is

$$Q = E_3 \left( 1 + \frac{m_3}{m_4} \right) - E_1 \left( 1 - \frac{m_1}{m_4} \right) - \frac{2\sqrt{m_1 m_3 E_1 E_3}}{m_4} \cos \Theta \quad (2)$$

where  $E_1$  = proton energy,  $E_3$  = neutron energy,  $m_1$  = proton mass,  $m_3$  = neutron mass,  $m_4$  = mass of residual nucleus and  $\Theta$  = angle of the emitted neutrons. It is seen that the masses appear only as ratios where small mass value errors would have little effect on the Q-value. This is in contrast to the value obtained from subtraction of masses where the difference of two nearly equal numbers is involved.

With the approximate correction to the neutron energy from observation of the  $F^{19}$  resonance, the narrow neutron resonances in strontium shown in Figures 12 and 13 could be identified.

The resonance at 110 keV (Bilpuch, et al., 1961) was used to make a final Q-value correction. With a width at half-maximum on the order of 500 eV, a very accurate correlation between neutron energy (110 keV) and proton energy at the peak could be made. Substitution into Eq. (2) gave a Q-value for the  $O^{18}(p,n)$  reaction of  $-2439 \pm 1.0$  keV which





Figure 12. Neutron Transmissions in Natural Strontium

$O^{18}(p,n)F^{18}$

NEUTRON TRANSMISSIONS IN NATURAL STRONTIUM

$\theta = 20^\circ$ ,  $\theta = 0.5^\circ$

SAMPLE THICKNESS = 0.0316 ATOMS / BARN

TRANSMISSION

$E_N$  IN keV

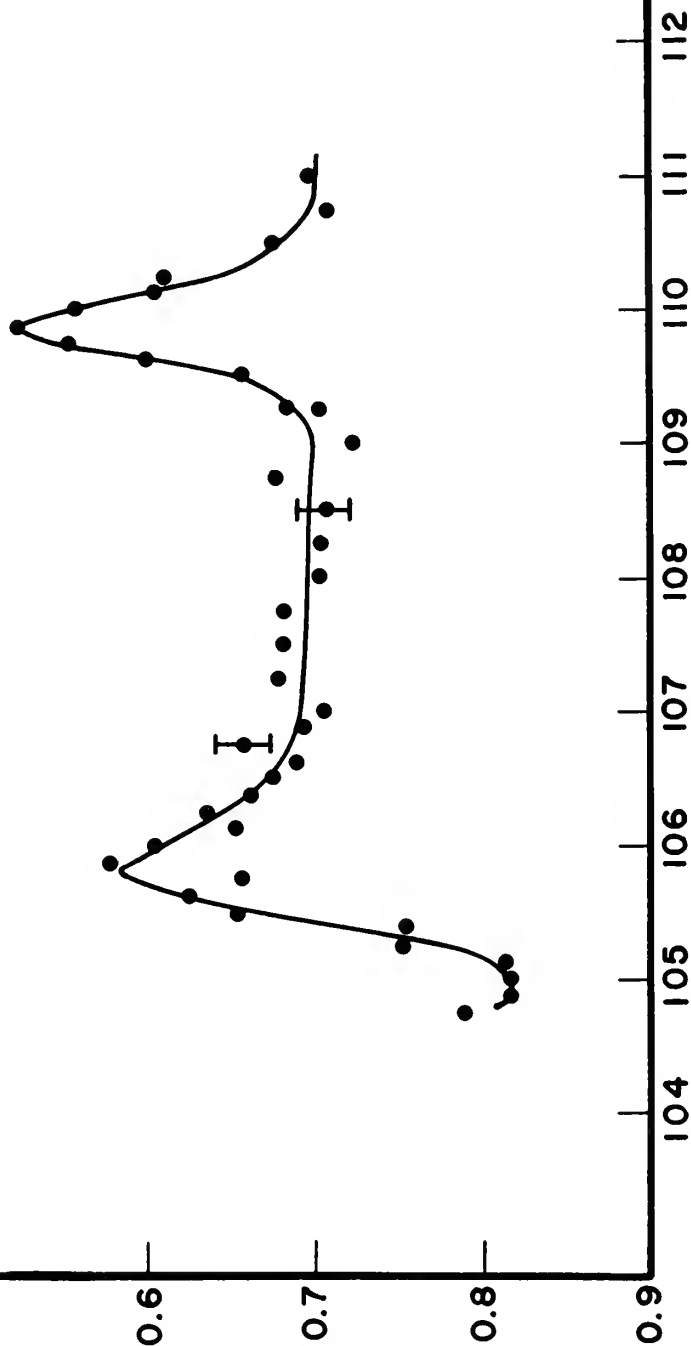
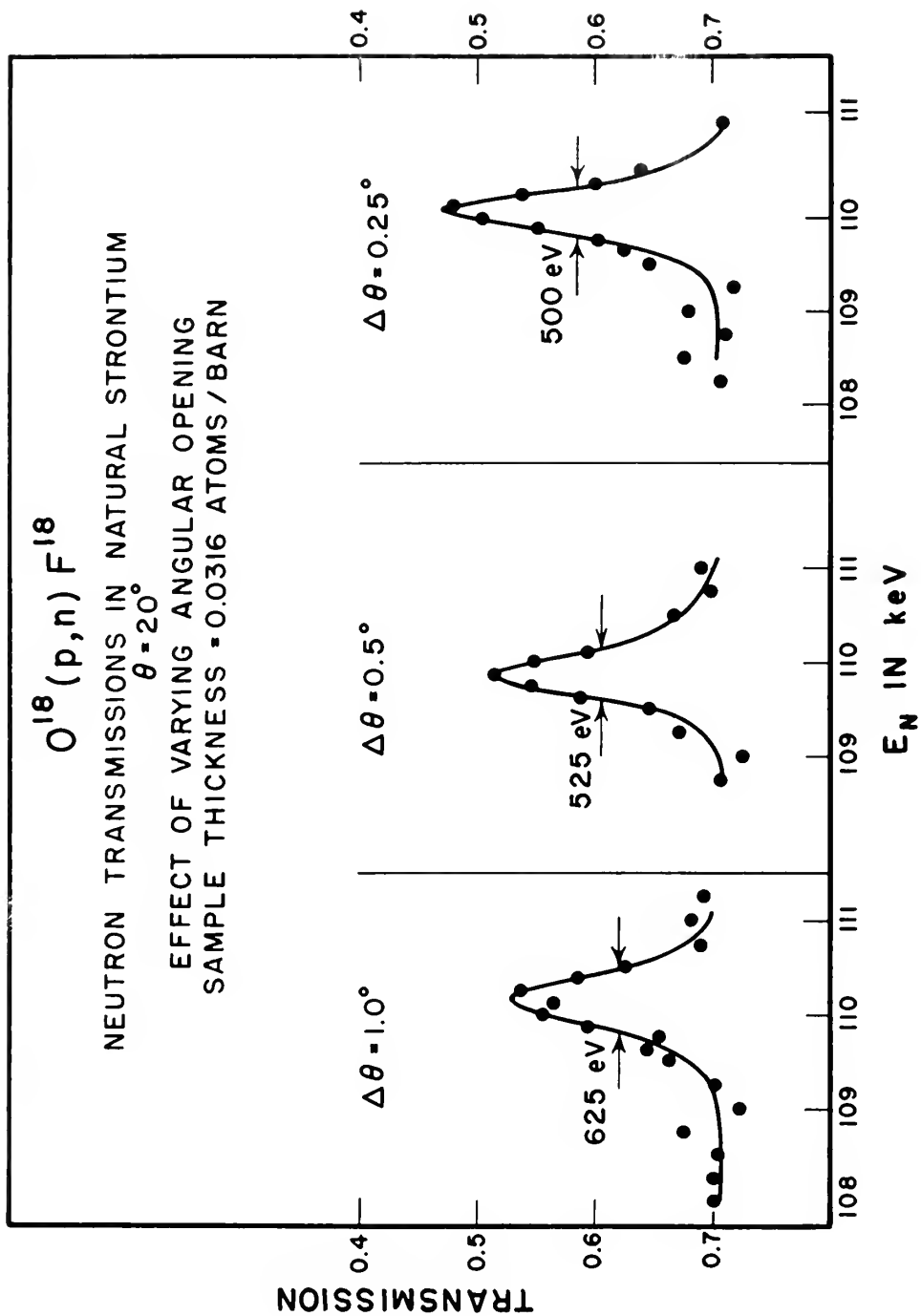








Figure 13. Neutron Transmissions in Natural Strontium.  
Shows effect of  $\Delta \Theta$  on neutron  
energy spread.





places reaction threshold (laboratory system) at  $2576 \pm 1.0$  keV. This may be compared with the value of  $2573.4 \pm 0.8$  keV reported by Bondelid and Butler (1964) based on the direct observation of a thick target yield. The difference involved is slightly greater than the stated limits of error. From our measured Q-value the mass excess of  $F^{18}$  on the  $C^{12}$  scale is computed to be  $874.1 \pm 1.0$  keV and the mass as 18.0009387 AMU. Everling, *et al.*, (1960) place the mass excess of  $F^{18}$  at  $884.8 \pm 4.3$  keV and the mass at 18.0009499 AMU.

With an accurate calibration of neutron energy, transmission measurements were then taken in natural potassium between 105 and 110 keV (Fig. 14) and in natural iron at the higher energy region (510-535 keV) as shown in Figure 15. The peak energy of each neutron resonance observed agreed with previously reported values within a keV. The data of Figure 15 is directly compared with the earlier work of Bowman, Bilpuch, and Newson (1962) where a solid  $Li^7$  target was used as the neutron source. The improvement by a factor of two in neutron energy resolution obtained with a gas target enabled the previously observed resonances at 512 and 532 keV to be resolved into two peaks. The error bars shown on all of the transmission data exhibit the influence of the relatively high background involved--see Chapter III.

## 2. Neutron Energy Resolution.

We can now examine the question of actual neutron energy resolution





Figure 14. Neutron Transmissions in Natural Potassium



# $^{18}\text{O}(\text{p}, \text{n})\text{F}^{18}$

NEUTRON TRANSMISSIONS IN NATURAL POTASSIUM

$\theta = 20^\circ$ ,  $\Delta\theta = 0.5^\circ$

SAMPLE THICKNESS = 0.0326 ATOMS/BARN

TRANSMISSION

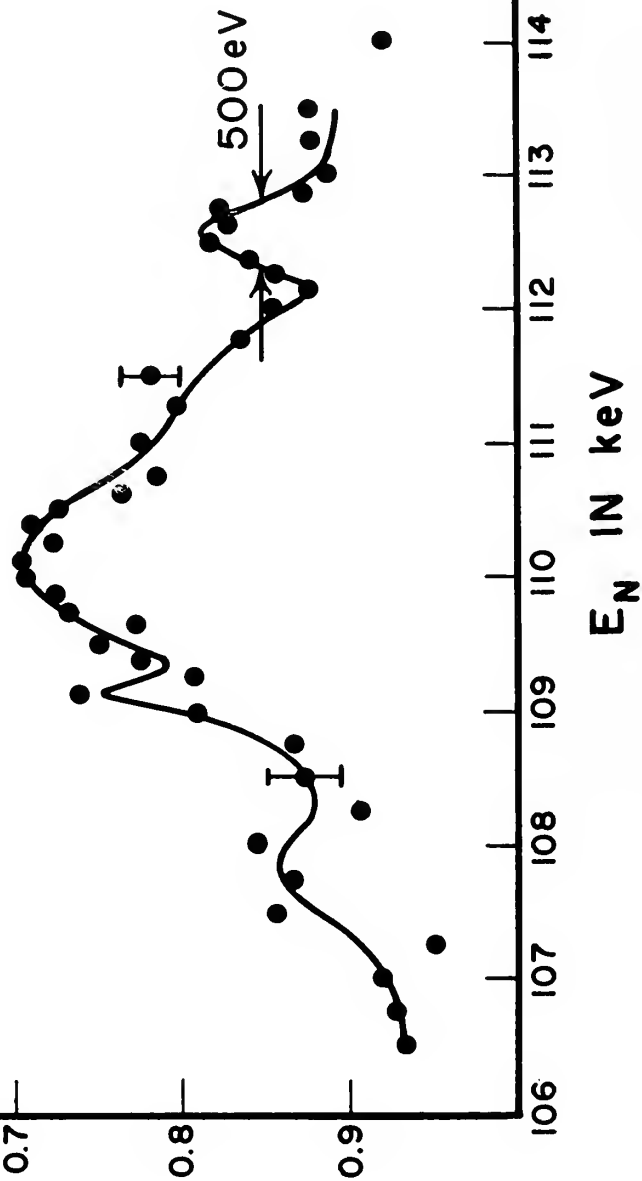






Figure 15. Neutron Transmissions in Natural Iron.  
Shows effect of improved resolution.



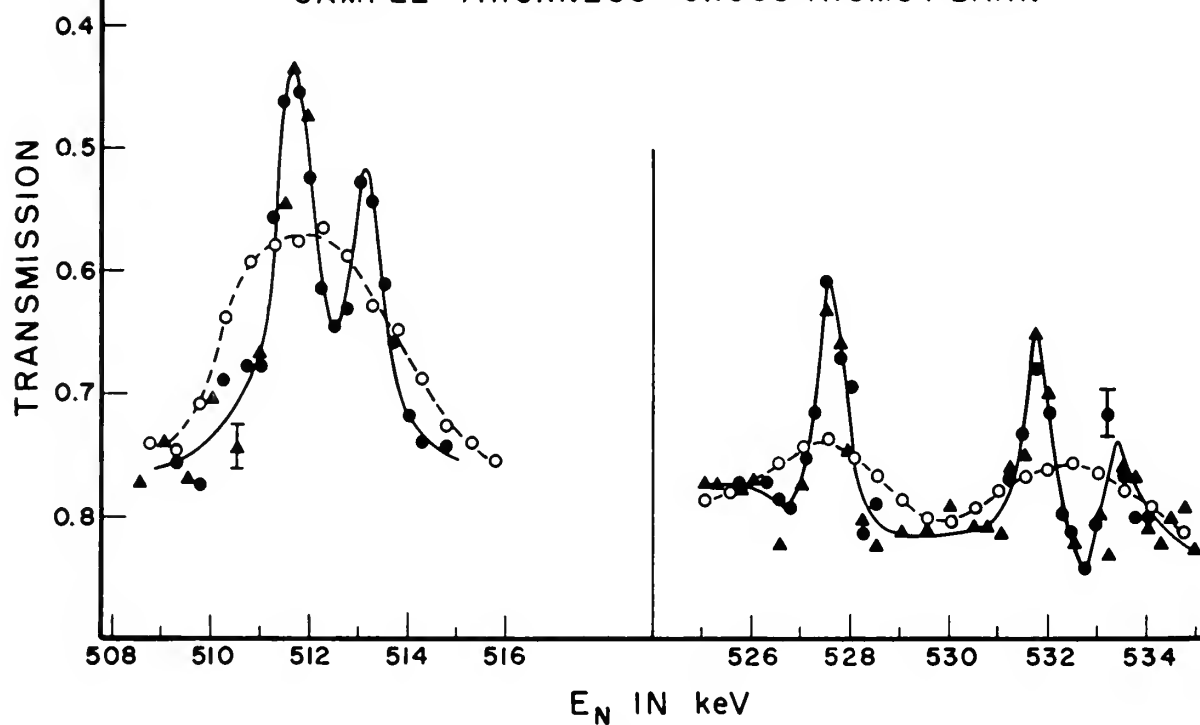
NEUTRON TRANSMISSIONS IN NATURAL IRON

$\theta = 20^\circ$ ,  $\Delta\theta = 0.5^\circ$

— PRESENT DATA

- - - PREVIOUS DATA TAKEN WITH  
SOLID LITHIUM TARGET

SAMPLE THICKNESS = 0.1068 ATOMS / BARN





attained as indicated from the  $20^\circ$  transmission data. The factors contributing to the width of the neutron energy distribution function are the incident proton energy spread, the target thickness (proton energy lost within the target), the finite angular opening to the counter banks, the Doppler effect due to the translational motion of the gas target atoms, and a Doppler effect from the vibrational motion of the di-atomic  $O^{18}$  molecule. We will neglect the finite length of our gas target and diameter ( $\sim 1/16''$ ) of the proton beam, both of which introduce unimportant angular errors.

By assuming or calculating the appropriate distribution functions for the various factors, they can then be combined to predict the effective width of the resultant neutron energy distribution. Detailed calculations and plots of resolution factors as a function of neutron energy are given in Appendix C. The incident proton distribution and the distribution introduced by proton energy loss in the target are assumed to be Gaussian. The half width (width at half maximum) of the incident proton distribution is taken to be  $1/11000$  of the proton energy as shown in Chapter III. The resultant contributions of these proton energy spreads to the neutron distribution are obtained by multiplying the appropriate widths by  $\partial E_n / \partial E_p$ . The ratio  $\Delta E_n / \Delta E_p$  is always greater than one at  $20^\circ$  and less than one at  $160^\circ$ .

The translational motion of the target atoms introduces an additional Gaussian distribution into the incident proton beam (Bethe and Placzek,





1937) as does the vibrational Doppler effect--see Appendix C.

The finite angular opening of the neutron collimator causes an energy spread in the neutrons admitted to the counters since the laboratory energy of the neutrons is a function of  $\Theta$ , the angle of the admitted neutrons as measured from the direction of the incident beam. This distribution function is rectangular in shape. In order to combine this spread with the other Gaussian distributions it may be represented by an equivalent Gaussian distribution whose half width is equal to .681 times the rectangular width (Nichols, 1958).

The half width  $\Delta$  of the Gaussian distribution resulting from the combination of several Gaussian functions each of half width  $\Delta_i$  is given by

$$\Delta = [ \sum_i (\Delta_i)^2 ]^{\frac{1}{2}} .$$

Thus our resultant neutron energy distribution function has a half width

$$\Delta_{E_n} = [ (\Delta_{E_p})^2 + (\Delta_t)^2 + (\Delta_{td})^2 + (\Delta_{vd})^2 + (.681 \Delta_{\Theta})^2 ]^{\frac{1}{2}}$$

where  $\Delta_{E_p}$  and  $\Delta_t$  are the equivalent neutron widths of the spreads due to incident proton inhomogeneity and target thickness resp.,  $\Delta_{td}$  and  $\Delta_{vd}$  are the neutron widths of the translational and vibrational Doppler spreads and  $\Delta_{\Theta}$  is the width of the rectangular angular distribution.  $\Delta_{E_n}$



varies of course with both  $E_n$  and  $\Theta$  as seen from the curves of Appendix C.

If this neutron energy spread is combined with a narrow isolated non s-wave Breit-Wigner resonance the resulting shape is essentially Gaussian. Hence from the half width of the transmission resonance the neutron energy spread may be estimated if the natural width,  $\Gamma$ , of the resonance is known. In this manner the predicted neutron resolution was checked against the observed widths of the non s-wave resonances in strontium at 110 keV and in iron at 528 keV--see Figures 12, 13, and 15.

$\Gamma$  is the width of the Breit-Wigner function when plotted as cross section versus energy. However in the lab we observe a resonance on a transmission versus energy scale where the relation between cross section,  $\sigma$ , and transmission,  $T$ , is given by

$$T = e^{-n\sigma}$$

for a sample of thickness  $n$  atoms/cm<sup>2</sup>. Therefore we need the equation relating  $\Gamma$  and the transmission half width  $\Delta$  of the resonance.

For a non s-wave resonance superimposed on s-wave potential scattering we can write

$$\sigma = \sigma_r + \sigma_p$$



Table 2. Neutron Energy Resolution,  $\Theta = 20^\circ$ 

Neutron Energy of Resonance	Natural Trans- mission Width	Predicted Neutron Energy Spread ( $\Delta \Theta = 0.5^\circ$ )	Observed Neutron Energy Spread
110 keV ( $\text{Sr}^{88}$ )	290 eV ( $g = 1$ ) 210 eV ( $g = 2$ )	415 eV	430 eV ( $g = 1$ ) 475 eV ( $g = 2$ )
528 keV ( $\text{Fe}^{56}$ )	395 eV ( $g = 1$ ) 190 eV ( $g = 3$ )	480 eV	515 eV ( $g = 1$ ) 620 eV ( $g = 3$ )



The non s-wave resonance in natural iron at 528 keV has been assigned to  $\text{Fe}^{56}$  (Bowman, et al., 1962). Assuming the possibility of d-wave neutrons, values of  $\Gamma$  from area analysis are given for  $g = 1$ , 2, or 3. The comparison between predicted and observed neutron resolution is given in Table 2 for  $g = 1$  and  $g = 3$ .

In both resonances we have good agreement for the  $g = 1$  case so that results of the  $20^\circ$  resolution work may be summarized by stating that the optimum observed neutron energy spreads at 110 keV and 530 keV can be only slightly greater than predicted values. Some improvement could probably be obtained by more accurate estimates of the incident proton spread and vibrational Doppler effect as well as by taking into account the effects of finite target length and possible imperfect alignment of the beam with the cone axis of the neutron collimator, but the agreement is practically within the uncertainty introduced by the unknown  $g$  factors.

### C. Neutron Transmission Measurements at $160^\circ$

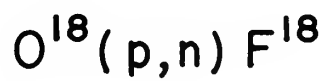
The results of the  $\text{O}^{18}(\text{p}, \text{n})$  neutron transmission measurements at  $160^\circ$  are shown in Figures 16 and 17. These indicate the neutron resolution around 28 keV where the yield of the  $\text{O}^{18}(\text{p}, \text{n})$  resonance at 2.643 MeV was utilized. Since measurements at this angle were primarily directed at determining the ultimate resolution possible with the gas target,







Figure 16. Neutron Transmissions in Cobalt



NEUTRON TRANSMISSIONS IN NATURAL COBALT

$\theta = 160^\circ \quad \Delta\theta = 0.5^\circ$

— PRESENT DATA

--- PREVIOUS DATA TAKEN WITH  
SOLID LITHIUM TARGET

SAMPLE THICKNESS = 0.0364 ATOMS/BARN

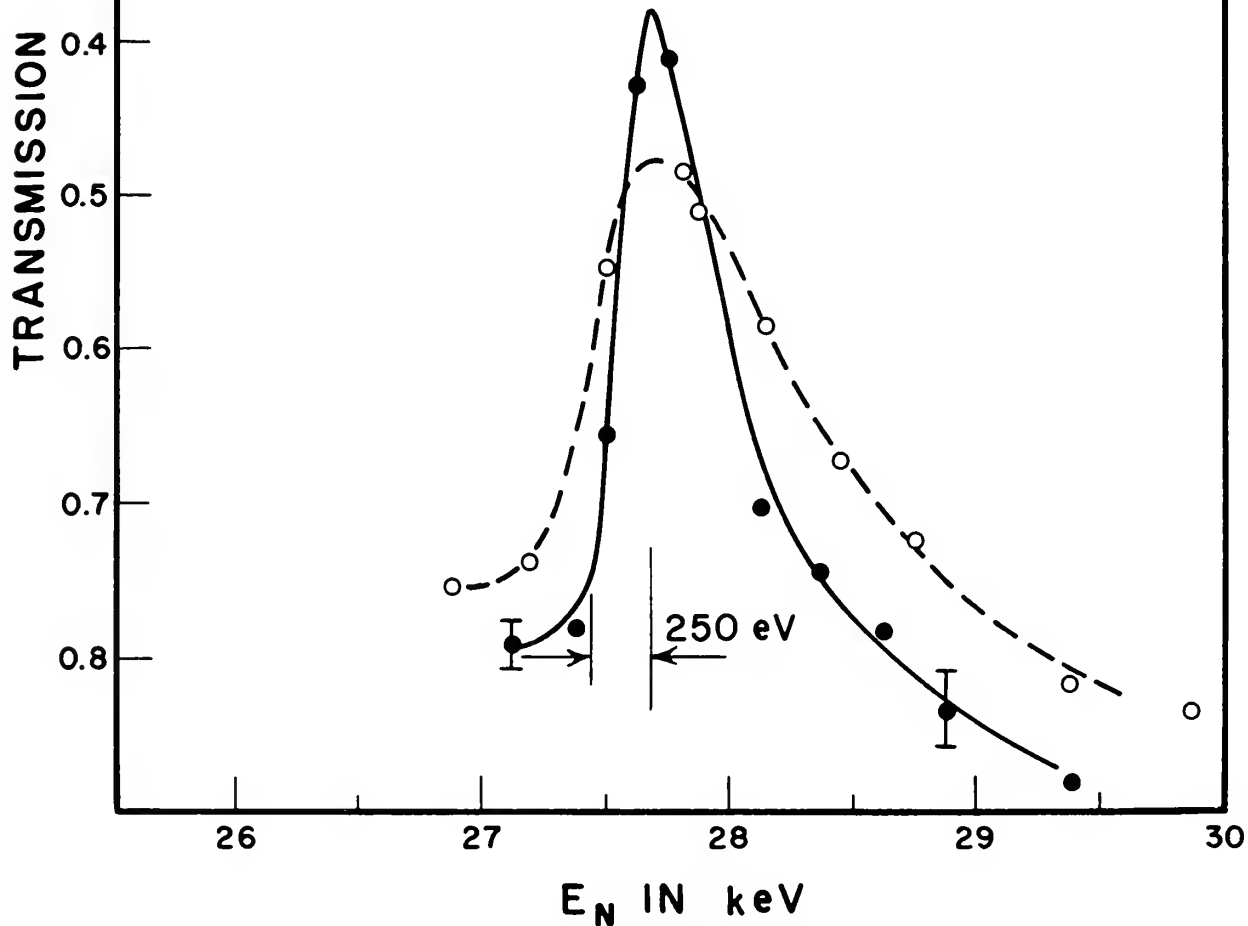
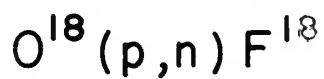






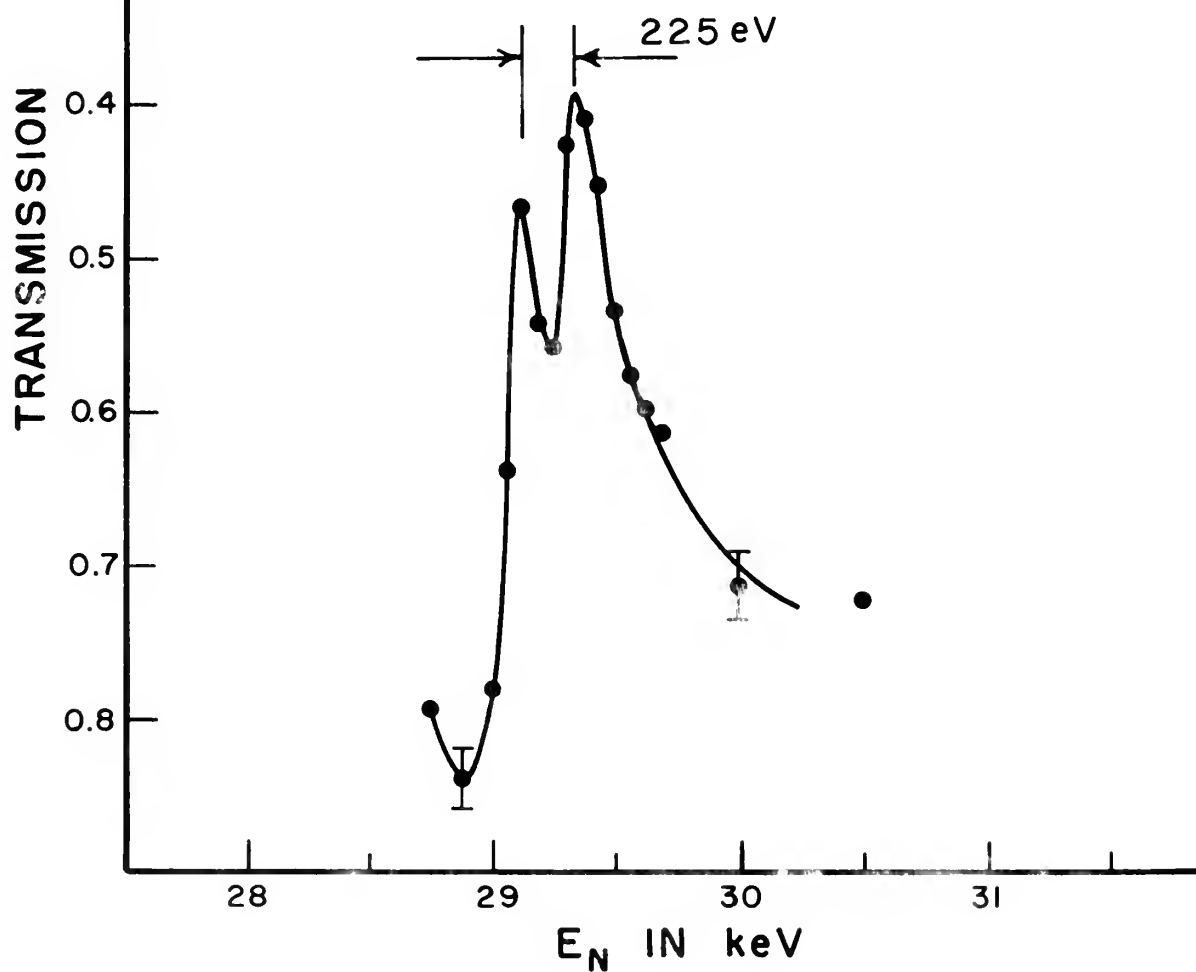
Figure 17. Neutron Transmissions in Yttrium



NEUTRON TRANSMISSIONS IN NATURAL YTTRIUM

$\theta = 160^\circ$ ,  $\Delta\theta = 0.5^\circ$

SAMPLE THICKNESS = 0.0448 ATOMS/BARN







most effort was spent in this lower energy region where the predicted neutron energy spread is only 210 eV for a  $0.5^\circ$  angular opening. As shown in Appendix C this spread increases to around 330 eV for neutron energies in the vicinity of 300 keV (i.e., the region of the  $3.025 \text{ MeV } O^{18}(p,n)$  resonance) which is not appreciably below that for  $20^\circ$ .

We first looked for a narrow resonance in natural copper between 27 to 29 keV. However the limitations of low yield and small target gas supply made such "scanning" extremely tedious. Even after taking  $1/8$  keV energy steps the resulting point scatter probably indicated the presence of resonances so narrow and closely spaced that no definite conclusions could be drawn. It was also a problem to repeat the observation of resonance widths on the order of 200 eV within a limited energy range of 3 keV when our proton energy calibration was good to only 1 keV. Hence it was decided that the previously measured resonance in natural cobalt at 27.5 keV (Bilpuch, et al., 1964) and the region in yttrium around 28 keV (Newson, et al., 1961b) would be most interesting.

The cobalt resonance is compared with earlier data taken with neutrons from a solid  $Li^7$  target (Fig. 16). Since this is an s-wave resonance the asymmetric shape partially masks the neutron energy spread estimated from a half width. Instead the slope of the rise from valley to peak is an indication of the neutron resolution. In Figure 16 this rise occurs in about 250 eV.



An alternative method for estimating the width of the resolution function involves comparing the maximum observed cross section of a resonance with the theoretical maximum. Feld, et al., (1951) have calculated the ratio  $\sigma_m^e/\sigma_m^t$  as a function of the ratio  $\Gamma/\Delta$  assuming a Gaussian resolution function. The theoretical maximum cross section  $\sigma_m^t$  is taken equal to  $4\pi\lambda^2g$  while the maximum observed cross section,  $\sigma_m^e$ , represents the difference in cross section between the dip and the peak of an s-wave. The natural width  $\Gamma$  of the cobalt resonance at 27.5 keV has been estimated to be 226 eV from area analysis (Bilpuch, et al., 1964). Our observed ratio of  $\sigma_m^e/\sigma_m^t$  was 0.66 and this gives  $\Gamma/\Delta = .88$ . Hence the estimated half width,  $\Delta$ , of our neutron resolution function is 255 eV according to this method.

The narrow resonances in yttrium (Fig. 17) were repeated several times although again some difficulty with the uncertainty in proton energy calibration was experienced. Even with a difference of 500 eV in neutron energy between runs, the target gas supply could be 2/3 depleted during a single run before enough points could be taken to identify the exact region being observed. All of the resonances studied were either too narrow or too closely spaced to be completely resolved but our neutron resolution was again demonstrated by an ability to separate resonance peaks less than 250 eV apart.

In Table 3 the comparison between the calculated and experimentally



Table 3. Neutron Energy Resolution,  $\Theta = 160^\circ$ 

Neutron Energy	Predicted Neutron Energy Spread, $\Delta \Theta = 0.5^\circ$	Estimated Neutron Energy Spread from $\text{Co}^{59}$ & Yttrium Resonances
30 keV	210 eV	$\leq 250$ eV



estimated resolution for  $160^\circ$  is shown. Although the evidence for the success of our resolution prediction was not as strong as for the  $20^\circ$  work, the agreement with experimental observation seems quite satisfactory since the cryogenic target chamber can apparently supply neutrons from the  $O^{18}(p,n)$  reaction with a total energy spread of around 200 eV.





## CHAPTER V

### CONCLUSIONS

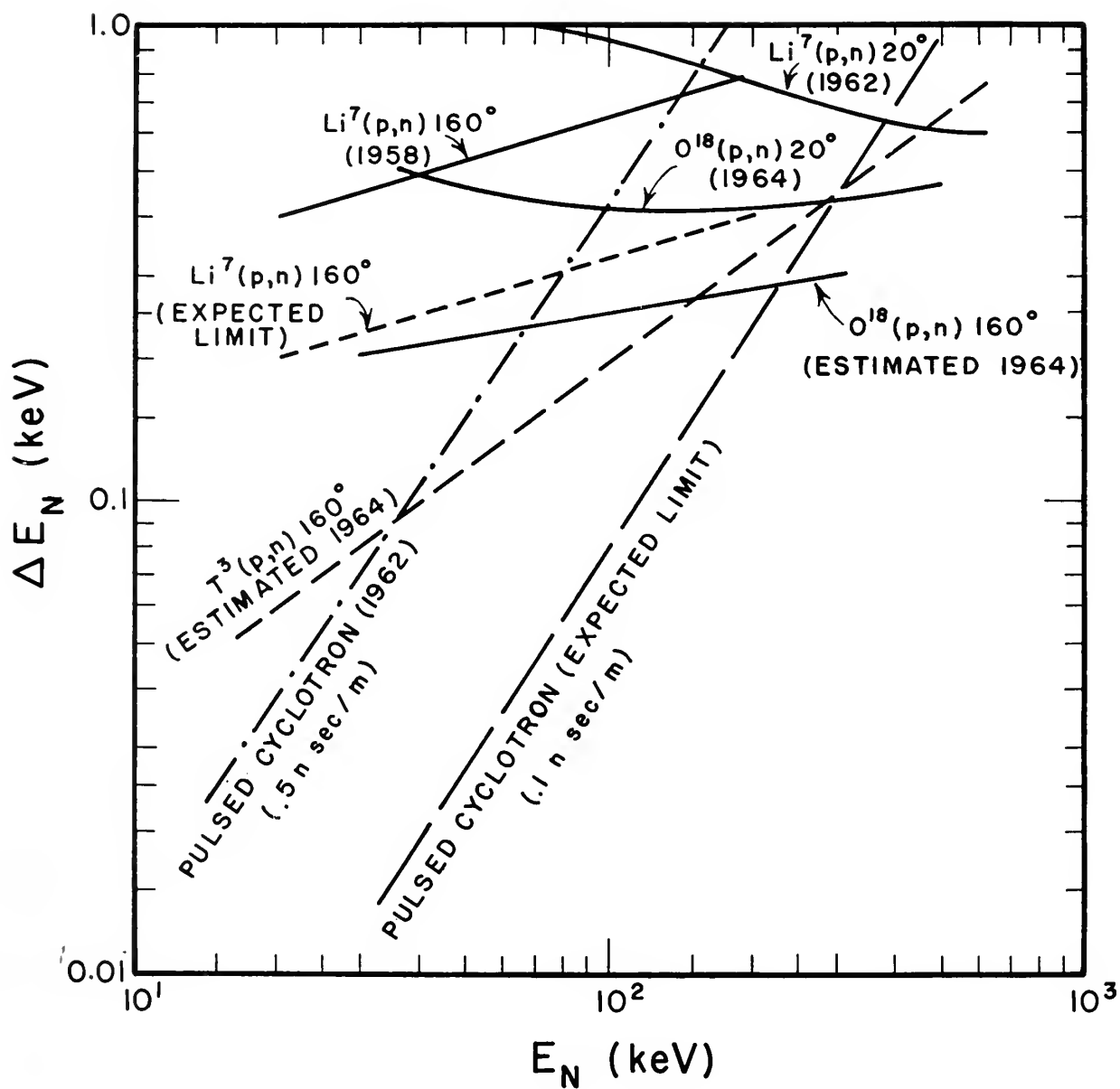
The applicability of the cryogenic target chamber in using a gas target as a high resolution neutron source has been demonstrated. The agreement between predicted and observed neutron energy resolution from the  $O^{18}(p,n)F^{18}$  reaction has been very good at  $\Theta = 160^\circ$  as well as at  $20^\circ$ . This is in contrast to experiences with a solid lithium target where, for  $160^\circ$ , the experimental resolution was about a factor of two worse than expected values (Nichols et al., 1959). Due to the low neutron yield between resonances the  $O^{18}(p,n)$  reaction is, of course, unsuitable as a neutron source in the keV range. However the  $T^3(p,n)He^3$  reaction with  $T_2$  gas in the target chamber should prove satisfactory for this purpose. The cross section for this reaction is continuous above threshold and comparable with that of  $Li^7(p,n)$ . Furthermore there is no low lying state in  $He^3$  to give rise to a second energy group of neutrons.

In Figure 18 the expected as well as the demonstrated resolution from the reactions  $T^3(p,n)$ ,  $O^{18}(p,n)$  and  $Li^7(p,n)$  are compared with the





Figure 18. Summary of Neutron Energy Resolution in the keV Region. Pulsed cyclotron curves are from Garg et al. (1964).





latest results of the Nevis pulsed cyclotron (Garg, Rainwater, and Havens, 1964). It is seen that at the present time the tritium gas target should afford better resolution than the pulsed cyclotron above 35 keV neutron energy. In addition it has the advantage of being able to be used with small samples of separated isotopes for transmission measurements. Above 350 keV the  $T^3(p,n)$  neutron energy spread is not significantly better than that attained at  $20^\circ$  with a solid lithium target. In analogy to the  $O^{18}(p,n)$  reaction the limiting factor on the resolution from  $T^3(p,n)$  at  $160^\circ$  should be the spread introduced from the vibrational Doppler effect--see Figure 27, Appendix C.

The feasibility of working with a limited supply of target gas has also been proven. The success of the recovery and handling system with oxygen gas should extend to tritium when the present gas reservoirs are replaced with uranium oven-type reservoirs. The only contamination problem with tritium should be that due to hydrogen, and trial experiments on the operation of the system can easily be performed with deuterium gas. The present design of the recovery and handling system should also prove useful with other gases. For example, a high resolution study of the  $C^{13}(p,n)N^{13}$  reaction near threshold could be made using methane gas,  $CH_4$ , enriched in  $C^{13}$ .

Finally this study of the  $O^{18}(p,n)$  reaction has demonstrated the need for better proton energy calibration. As discussed before, the accuracy of threshold measurements by the neutron transmission method





is limited by the present method of calibration. Furthermore, in making high resolution measurements of neutron resonances with an energy spread of  $\leq 100$  eV from  $T^3(p,n)$ , one would be seriously hampered by an inability to reproduce proton energies better than 1 keV.



## APPENDIXES



## APPENDIX A

### RARE GAS HANDLING AND RECOVERY SYSTEM

The rare gas handling and recovery system table was shown in Figure 3, p.15 and a schematic diagram of the entire system appears in Figure 19. The table is 30 in. wide, 60 in. long, and stands approximately 44 in. from the floor. It is equipped with wheels for positioning and screw-type jacks for final height adjustment. The table frame consists of steel angle iron with 1/2 in. aluminum plates for the top and bottom. Each of the major pieces of equipment is attached to the table top with flanges drilled and tapped for 1/4 - 20 screws. Thus any piece may be easily removed for repairs or replacement.

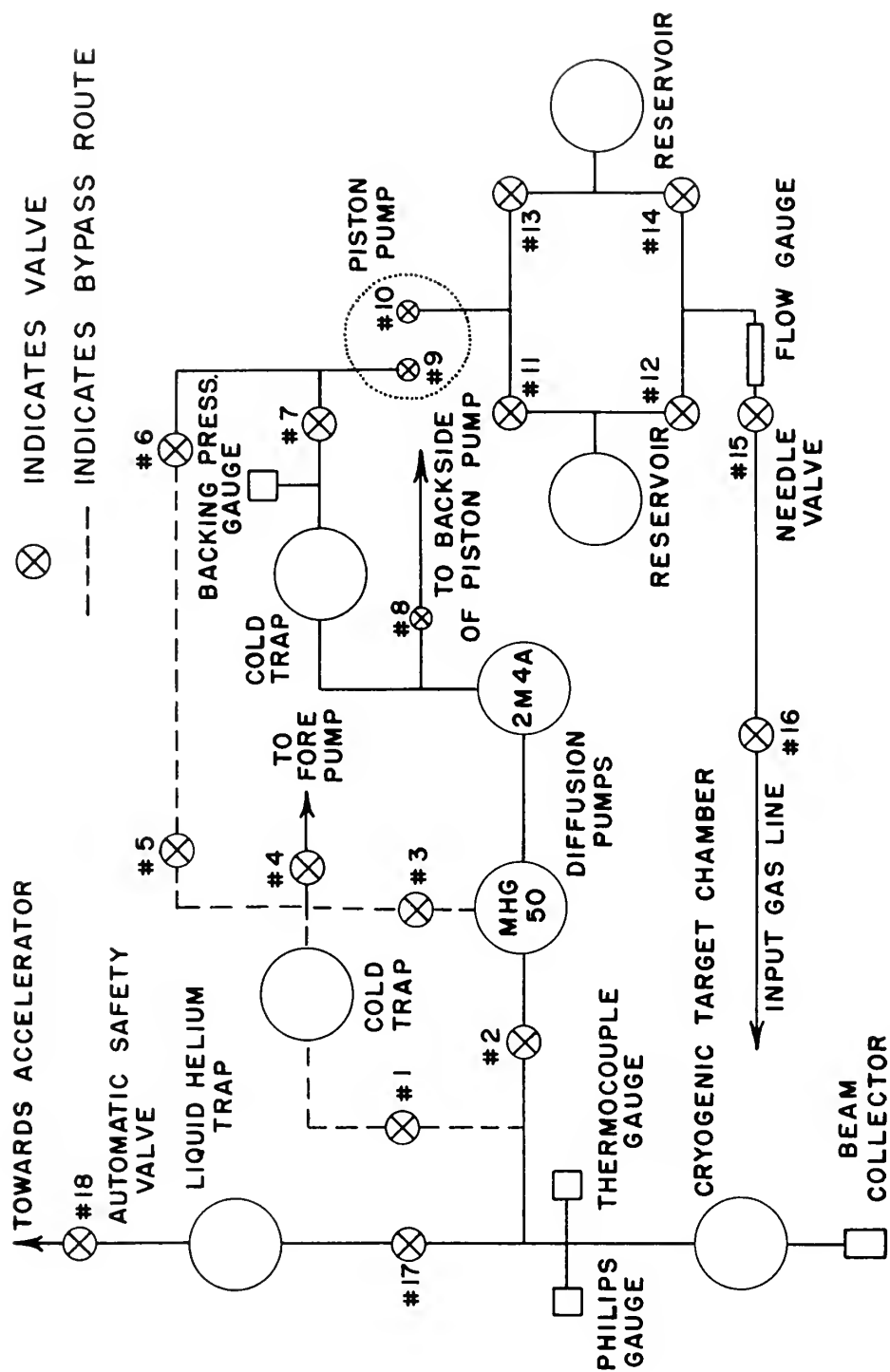
The associated plumbing is constructed entirely of metal with connections made by means of threaded couplings employing O-rings. For ease in assembly, stainless steel bellows are used in selected pieces of tubing to allow for errors in aligning. The entire plumbing system may be taken apart or re-assembled without having to break into permanent solder or weld joints.





Figure 19. Rare Gas Handling and Recovery System Diagram





HANDLING AND RECOVERY SYSTEM DIAGRAM



To prevent future contamination of neoprene rubber O-rings and surfaces with tritium or other radioactive gases, teflon O-rings and valve seats are used wherever possible. With the exception of the VRC two inch gate valve (valve #2 on the diagram) all valves are of bellows-type construction with brass bodies and stainless steel bellows. Several fittings are made with 1/4 NPT joints with teflon tape wrapped on the threads to insure a vacuum tight connection.

There was also some concern over the possibility of mercury, from the diffusion pumps, attacking solder joints. Thus all surfaces in constant and direct contact with mercury vapor were nickel plated. This included the traps above the diffusion pumps as well as the other cold traps in the system.

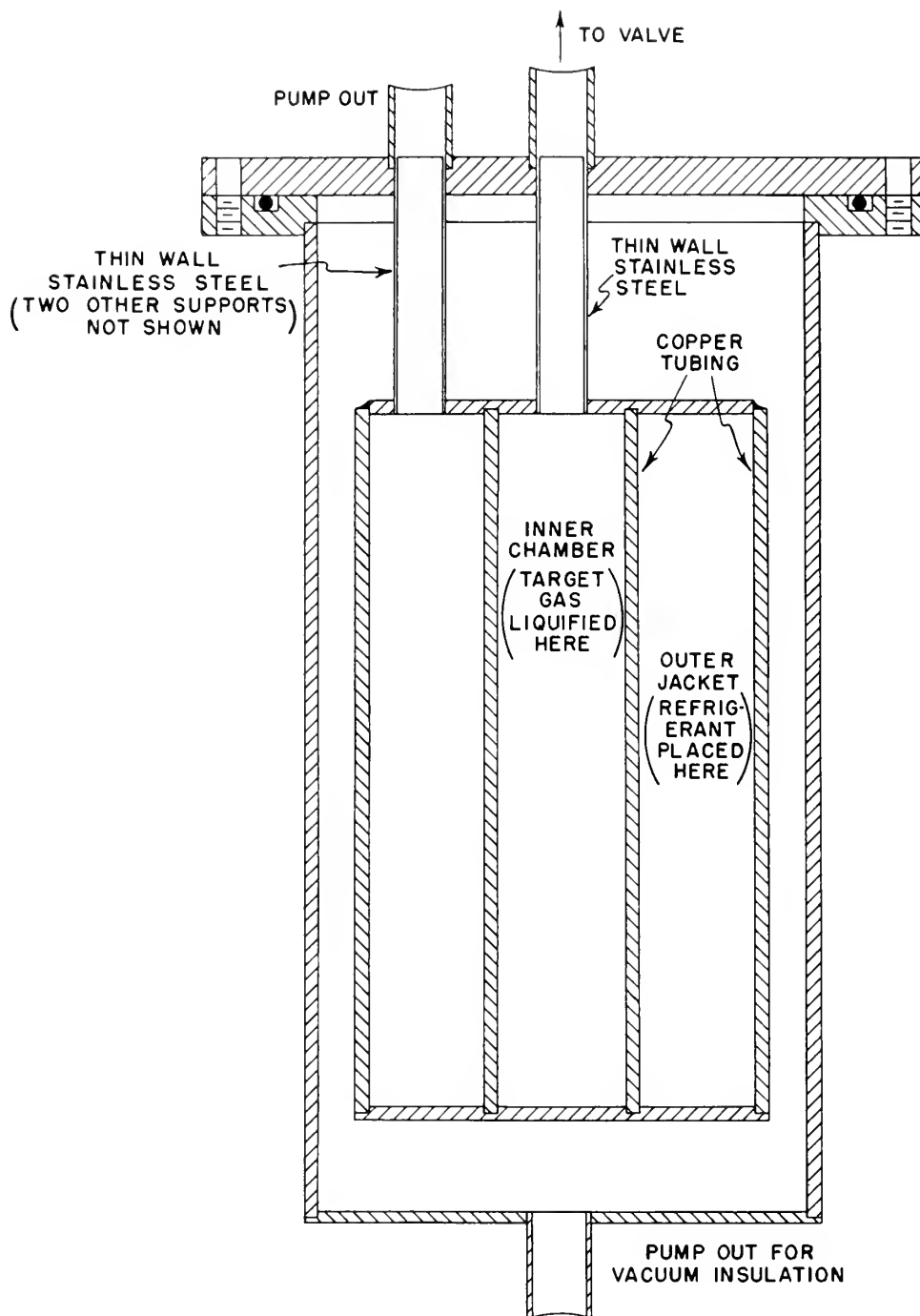
The main pumping action is provided by a CVC Type MHG-50 two-stage mercury diffusion pump with a speed of 50 liters/sec. The backing pump is an Edwards High Vacuum model 2M4A four-stage mercury diffusion pump. This pump is designed to withstand a backing pressure on its output side of up to 35 torr (i.e., 35 mm. Hg). This capability is most important in a closed system where there is no fore pump exhausting to the atmosphere.

After passing through the diffusion pumps the oxygen gas (65% enriched in  $O^{18}$ ) is recovered by liquification in a gas reservoir--see Figure 20. The outer jacket surrounding the inner container of the gas reservoir is filled with liquid nitrogen at reduced pressure. In this manner





Figure 20. Gas Reservoir



GAS RESERVOIR





the temperature of the liquid nitrogen is lowered from  $77^{\circ}\text{K}$  to around  $56^{\circ}\text{K}$ . The oxygen is liquified upon reaching the inner container and, at  $56^{\circ}\text{K}$ , its vapor pressure is approximately 2 torr which is well below the backing pressure tolerance (35 torr) of the 2M4A diffusion pump and allows for considerable contamination from other gases such as nitrogen.

There must be two gas reservoirs in the system. The reservoir in which the gas was recovered from a previous run must then be the supply source for the succeeding run while the other reservoir serves for recovery. The vacuum insulation between the main bodies of the reservoirs and the cold surfaces is maintained with a small oil diffusion pump and roughing pump not shown in the diagram of Figure 19, p. 84. When tritium is to be used in the system the gas reservoirs would simply be replaced by uranium oven reservoirs (Johnson and Banta, 1956).

During a run the oxygen gas must be delivered to the cryogenic target chamber at a constant rate. The gas flow is regulated with a Hoke needle valve and measured directly in cc/min. with a Hoke #995 Bantam Flo-gage. However, in order to maintain a constant flow rate, the pressure before the needle valve must be held constant. As suggested by Newson (1963) this is accomplished in the following manner. The outer jacket of the reservoir containing the oxygen gas is filled with liquid oxygen. The oxygen in the inner chamber of this reservoir then becomes a liquid at  $90^{\circ}\text{K}$  (the boiling point) and the vapor pressure above the liquid will remain constant at one atm. until no liquid remains. The Flo-gage,



which requires essentially atmospheric pressure on its downstream side, is placed before the needle valve. This method of gas flow control has proven quite successful.

With only one liter (NTP) of oxygen gas available, the volume before the needle valve had to be kept very small in order to hold the constant vapor pressure as long as possible. The volume of the inner chamber proper is 240 cc which was reduced to 120 cc by filling it with stainless steel ball bearings. With this volume, approximately 70% of the oxygen should be initially liquified and, at 10 cc/min, a constant gas flow could be maintained for around 1  $\frac{1}{2}$  hours.

When confined to such a small volume, the pressure of the gas at room temperature rises to 100 psi or more. This factor was taken into account in the design of the system where a considerable safety margin was allowed. Small Ashcroft gauges are mounted on the top of each reservoir which read the pressures in the inner chambers.

The backing pressure of the 2M4A diffusion pump (or the vapor pressure of the recovered target gas plus contaminants) is accurately monitored with a Veeco vacuum gauge type SP-1 whose effective range is from 100 microns to 20 millimeters of mercury. If for some reason during a run this pressure were to rise above tolerable limits it could be reduced by means of the manual piston pump--see Figure 19, p. 84. This pump consists of a brass cylinder machined to a very close tolerance with a brass disc for a piston attached to a stainless steel stem. A rubber O-ring around



the outside of the piston affords a vacuum seal as the piston slides within the cylinder. Intake and exhaust valves are provided at the top of the pump and its volume is such that a single stroke of the piston reduces the backing pressure by a factor of two. The backside of the piston is maintained at vacuum by a small copper line leading to the input of the 2M4A diffusion pump.

The traps above the diffusion pumps are filled with  $\text{CO}_2$  (dry ice) at reduced pressure in order to insure condensation of most of the mercury as well as other vapors present in the system. The two additional traps shown in Figure 19, p. 84, are filled with a mixture of  $\text{CO}_2$  and acetone in order to catch any remaining mercury or oil vapor. An outlet valve to a roughing pump is provided for initial evacuation of the system.

The input to the main diffusion pump is connected to the section of beam pipe leading immediately into the cryogenic target chamber by two inch copper tubing and a two inch VRC gate valve. A thermocouple gauge as well as a Philips gauge indicate the vacuum at this point. The Philips gauge controls the operation of the automatic safety valve as described in Chapter II. Before introducing gas into the cryogenic target chamber the pressure in the chamber is maintained at about  $10^{-5}$  torr.

Referring to Figure 19, p. 84, the operation of the handling and recovery table during a complete cycle of the gas may be described as follows. At the start of a run all of the oxygen is contained in one of the gas reservoirs which is designated the supply reservoir. The other will be



referred to as the recovery reservoir. With the bypass line closed off with valves #1, #3, and #6 and with the main line open to the recovery reservoir, gas is fed from the supply reservoir to the cryogenic target chamber via a 1/4 inch copper line. Most of the gas leaving the reaction tubes of the target chamber is condensed on the outer trapping cylinders at liquid helium temperature (Parks et al., 1964). The small fraction of gas escaping into the beam pipe is subject then to the pumping action of the recovery system. Any remaining gas diffusing up the beam pipe toward the accelerator should be condensed on the liquid helium trap (Chapter II).

At the end of the run most of the gas is condensed on the trapping cylinders of the target chamber. Any remaining in the supply reservoir is transferred directly to the recovery reservoir through valves #12 and #14. If the small amount of gas collected on the liquid helium trap is to be recovered at this time, valve #18 is closed while the trap is warmed up to release its gas.

After all of the gas is condensed in the cryogenic target chamber (except for that part already pumped to the recovery reservoir) valve #17 is closed. If the cryogenic target chamber were to be warmed up now, the large amount of gas released would ruin the diffusion pump vacuum and cause mercury vapor to be spread around the system. Instead the bypass line is utilized. The diffusion pumps are isolated by closing valves #2 and #7. The cryogenic target chamber is warmed up by blowing





the liquid helium out of the main refrigerant container with compressed air and the bypass line is connected by opening valves #1 and #6. The released gas thus has a direct route to the recovery reservoir. Valve #5 is actually superfluous to this operation and is always left open.

After waiting several minutes for the bypass line pressure to reach equilibrium at the vapor pressure of the oxygen gas plus contaminants at 56°K, valve #6 is closed, valve #7 is opened and the diffusion pumps are connected slowly by opening valve #3. During this period of poor vacuum, only the thermocouple gauge can be used. When a vacuum of around  $5 \times 10^{-3}$  torr is reached, the Philips gauge is turned back on and the main gate valve, #2, is opened. Within 15 minutes the vacuum is on the order of  $5 \times 10^{-5}$  torr and the final step of the recovery may be undertaken.

This involves using the manual piston pump to force the gas between the output of the 2M4A diffusion pump and the intake valve of the pump into the recovery reservoir. The amount of "dead space" between the exhaust valve of the pump and the recovery reservoir was kept at a minimum. When the backing pressure gauge reads 0.2 torr the recovery operation is considered complete. It was found that this entire procedure could be carried out within 45 minutes.

The only major problem anticipated with the use of the handling and recovery system was the contamination of the oxygen with other gases such as air from leaks and hydrogen from the source bottle of the accelerator.



During assembly and at frequent intervals thereafter the entire system was carefully tested for air leaks. Of course hydrogen contamination from the source bottle was unavoidable but this was only a minor problem.

After the initial recovery cycle of the oxygen gas the backing pressure was about 2 torr which indeed corresponds to the vapor pressure of oxygen above the liquid at  $56^{\circ}\text{K}$ . As the experiment continued it was noticed that the backing pressure at the end of a recovery cycle continued to rise, but at a slow rate. This indicated, of course, that some contamination of the gas was taking place. At the end of the experiment, after more than 40 cycles of the gas had been completed, the backing pressure had increased to nearly 12 torr. This represents a total contamination of the gas of 10%.

This contamination could at any time have been reduced to a negligible value by isolating the recovery reservoir and then pumping out the remaining volume behind the 2M4A diffusion pump with a roughing pump through valve #4. Only a small part of the oxygen gas (1.0 percent) would be lost in this process. Also a small amount of condensable contaminants would remain in the recovery reservoir. Nevertheless the contamination problem can be kept under control at the cost of negligible amounts of the target gas.

Another consideration was the loss of target gas which was not condensed in either the cryogenic target chamber or the liquid helium trap and escaped up the beam pipe. It was determined experimentally that in a



single cycle about 1.5 % of the gas was picked up by the liquid helium trap but that an immeasurably small amount was lost. Again, after more than 40 cycles of the gas, the total loss from all causes was about 5.0 % or about 0.125 % per gas cycle.



## APPENDIX B

### OPERATION OF THE CRYOGENIC TARGET CHAMBER

Since different gases may vary widely in their thermodynamic properties, the operation of the cryogenic target chamber must be adjusted to suit the particular gas being considered. The following will explain the procedure for determining how oxygen gas should be used in the target chamber. The calculations for oxygen will then be compared with experimental results.

Before any gas can be used in the cryogenic target chamber for the first time, we must be able to estimate the temperature at which to operate the target chamber, the lifetime of the main refrigerant, the expected target gas density, and the necessary properties of the refrigerants and temperature gradient rod. In order to do this we must know the following thermodynamic properties of the gas under standard conditions: (1) boiling and melting points, (2) heats of vaporization and fusion, (3) specific heats of the gaseous, liquid, and solid phases and also, (4) the vapor pressure above the liquid and solid states as a function of temperature.





Properties (2) and (3) are necessary of course in determining the amount of heat delivered to the cryostat by the incoming gas while (4) is used to calculate the theoretical loss rate of the gas from the reaction tubes and the predicted target gas density within the tubes.

From the boiling and melting points we can choose the refrigerants to use in the cryostat. Referring to Figure 1, p. 8, the radiation shield refrigerant should be such that the incoming gas can be pre-cooled to minimize the amount of heat delivered to the main refrigerant by the gas. Of course excessive cooling would lead to condensation and possible blockage of flow in the gas line. However it has been found that it is actually possible for this refrigerant to be several degrees colder than the boiling point of the gas involved due to the low pressure in this line. The main refrigerant must maintain a temperature low enough that nearly all of the gas which escapes from the reaction tubes will condense upon the trapping cylinders (Parks et al., 1964). For natural oxygen the boiling and melting points are  $90^{\circ}\text{K}$  and  $54.6^{\circ}\text{K}$  respectively. Consequently liquid nitrogen at  $77^{\circ}\text{K}$  and liquid helium at  $4.2^{\circ}\text{K}$  were used as the refrigerants.

Predicting the operating temperature (the temperature at which to maintain the inner chamber consisting of the reaction tubes and cooling cavity) is the most important problem in preparing to use the cryogenic target chamber. This temperature should be several degrees warmer than that necessary to prevent condensation of the gas within the inner chamber



since we actually will operate under a condition of dynamic equilibrium between the input rate of the gas to the cooling cavity and the escape rate from the reaction tubes. This operating temperature may be conveniently estimated by a graphical determination of the point at which the theoretical escape rate from the reaction tubes is approximately equal to the input rate.

In explaining this method we must remember the effect of the temperature gradient rod as described in Chapter II. First we calculate the temperature to which different input gas flows would raise the inner chamber without any electrical power. As a first approximation, the heat input from the gas flow is given by

$$H = [ \bar{c}_p (T_i - T) + \lambda_v + \lambda_f ] GB \quad \text{watts} , \quad (4)$$

where  $G$  = gas flow in cc/min.,  $\bar{c}_p$  = average specific heat of the gas over the range  $T_i$  to  $T$ ,  $T_i$  = the temperature of the entering gas which is the same as the temperature of the radiation shield refrigerant,  $T$  = inner chamber temperature,  $\lambda_v$  and  $\lambda_f$  are the heats of vaporization and fusion resp. and  $B = 3.11 \times 10^{-6}$  joules - mole/cal. - sec. Here we have assumed that the incoming gas is condensed within the inner chamber.

From page 6, Chapter II, we have the equation for heat flow through the gradient rod

$$H = \frac{\bar{K}A}{L} (T - T_f) \quad \text{watts} . \quad (1)$$

Hence from Equations (1) and (4) we can solve for inner chamber temperature



as a function of input gas flow. A plot of this dependence is then made.

Assuming the pressure in the inner chamber to be the vapor pressure above the condensed gas, the theoretical escape rate of the gas from the reaction tubes of length  $L$  and radius  $R$  is given by the following equation (Parks et al., 1964):

$$N = 2PA (p-p_2)/m [ M/(2\pi R_o T) ]^{\frac{1}{2}} \text{ molecules/sec. ,}$$

where  $T$  = inner chamber temperature,  $p$  = inner chamber pressure,  $p_2$  = pressure at exit end of reaction tube which is assumed to be negligible,  $m$  = mass of molecule,  $M$  = molecular weight,  $A$  = tube cross sectional area and  $P$  is a parameter dependent on the ratio  $L/R$ . For our case  $L/R = 5$  and  $P = 0.31$ . On the same graph used for the plot of inner chamber temperature versus input rate we also plot the escape rate versus temperature. The point of intersection of these two curves gives us the predicted minimum temperature where, for gas flow heating alone, no condensation can take place within the inner chamber. Above this temperature the escape rate will always equal any possible input rate. For future reference the temperature at which the gas escape rate first becomes equal to a given input rate will be called the "break-point" of that input rate.

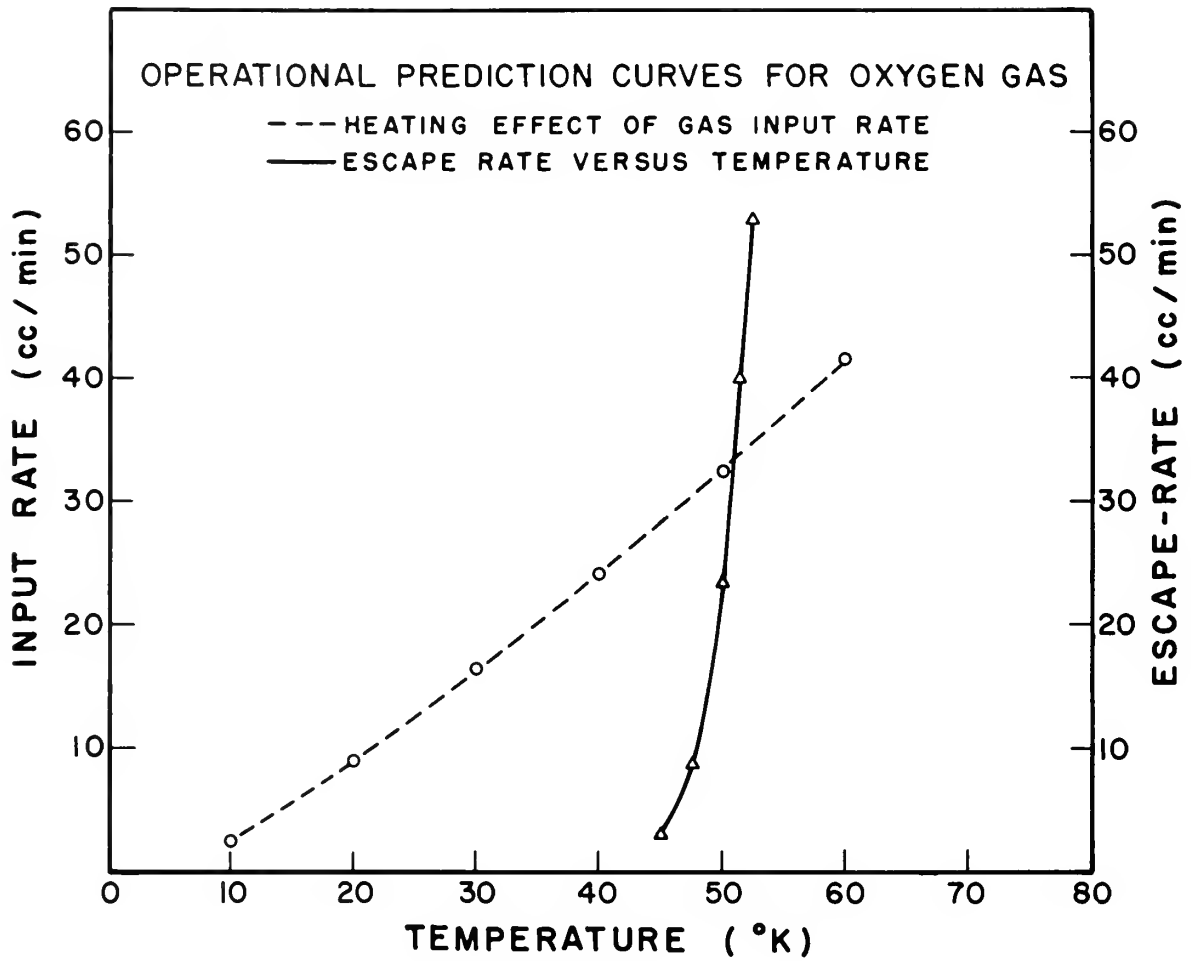
The graph used for oxygen gas is shown in Figure 21. Since the slope of the input curve is essentially determined by the  $\bar{K}A/L$  factor of the gradient rod used, the break-point may be varied several degrees by adjusting the material and geometry of the rod. This slope should be





Figure 21. Operational Prediction Curves for Oxygen Gas  
in the Cryogenic Target Chamber. Used for  
break-point predictions.







great enough such that the largest expected gas flow does not raise the temperature of the inner chamber more than a few degrees above that necessary to prevent condensation.

Again referring to Figure 21 it is possible to attain a break-point for gas flows smaller than 33 cc/min. (where the curves cross) simply by using the target heater. For example, with an input rate of 15 cc/min., we would reach a temperature of  $28^{\circ}\text{K}$  from the heating effect of the gas flow alone. Then by supplying electrical power to the target heater we can raise the temperature to  $40^{\circ}\text{K}$  where the escape rate becomes equal to the input rate. By operating several degrees above this break-point we can be assured that no condensation is taking place within the inner chamber. In actual practice with oxygen and other gases the target heater is always used in this manner. In particular, with oxygen, input rates of 5 to 30 cc/min. could be used without having to change the gradient rod.

The only experimental evidence we have for the success of the predicted operating point is the observation of target density as a function of temperature when the temperature is controlled by both the target heater and input gas flow. For the oxygen (65% enriched in  $\text{O}^{18}$ ) the relative total yield of the  $\text{O}^{18}(\text{p},\text{n})\text{F}^{18}$  reaction was measured under various conditions, with the proton energy set at the peak of the 2.643 MeV resonance (Fig. 9, p. 42). This yield, of course, was proportional to the density of the gas target within the reaction tubes. The temperature of the inner chamber was measured with a calibrated carbon resistor "thermometer" (Parks



et al., 1964) shown in Figure 2, p. 10. Referring to Figure 22, the solid curve represents the behavior of target density where, for a relatively small input gas flow (5 cc/min.) electrical heating was used to obtain the "break-point temperature" in the inner chamber. As indicated, this occurred at about  $48^{\circ}\text{K}$  where further electrical heating could not produce a denser target since the escape rate of the gas had become equal to the fixed input rate. The escape rate curve of Figure 21 predicts an escape rate of 5 cc/min. at  $46^{\circ}\text{K}$  which is in good agreement with the data considering the accuracy of the calculations. Between  $37^{\circ}$  and  $43^{\circ}\text{K}$  there is almost total condensation of the incoming gas within the inner chamber. At these temperatures we essentially have a "vapor pressure target" whose density increases quite rapidly with temperature as evidenced in the data. The dashed line gives the actual temperature variation of oxygen vapor pressure above the solid. Between  $43^{\circ}$  and  $48^{\circ}\text{K}$  we have a transition region where the density increases less rapidly with temperature due to the fast increase in the escape rate of the gas from the reaction tubes. Indeed, the point where the data draws away from the vapor pressure curve corresponds to the temperature at which the theoretical loss rate becomes appreciable--see Figure 21. Then, of course, above  $48^{\circ}\text{K}$  a condition of dynamic equilibrium is reached where no condensation takes place.

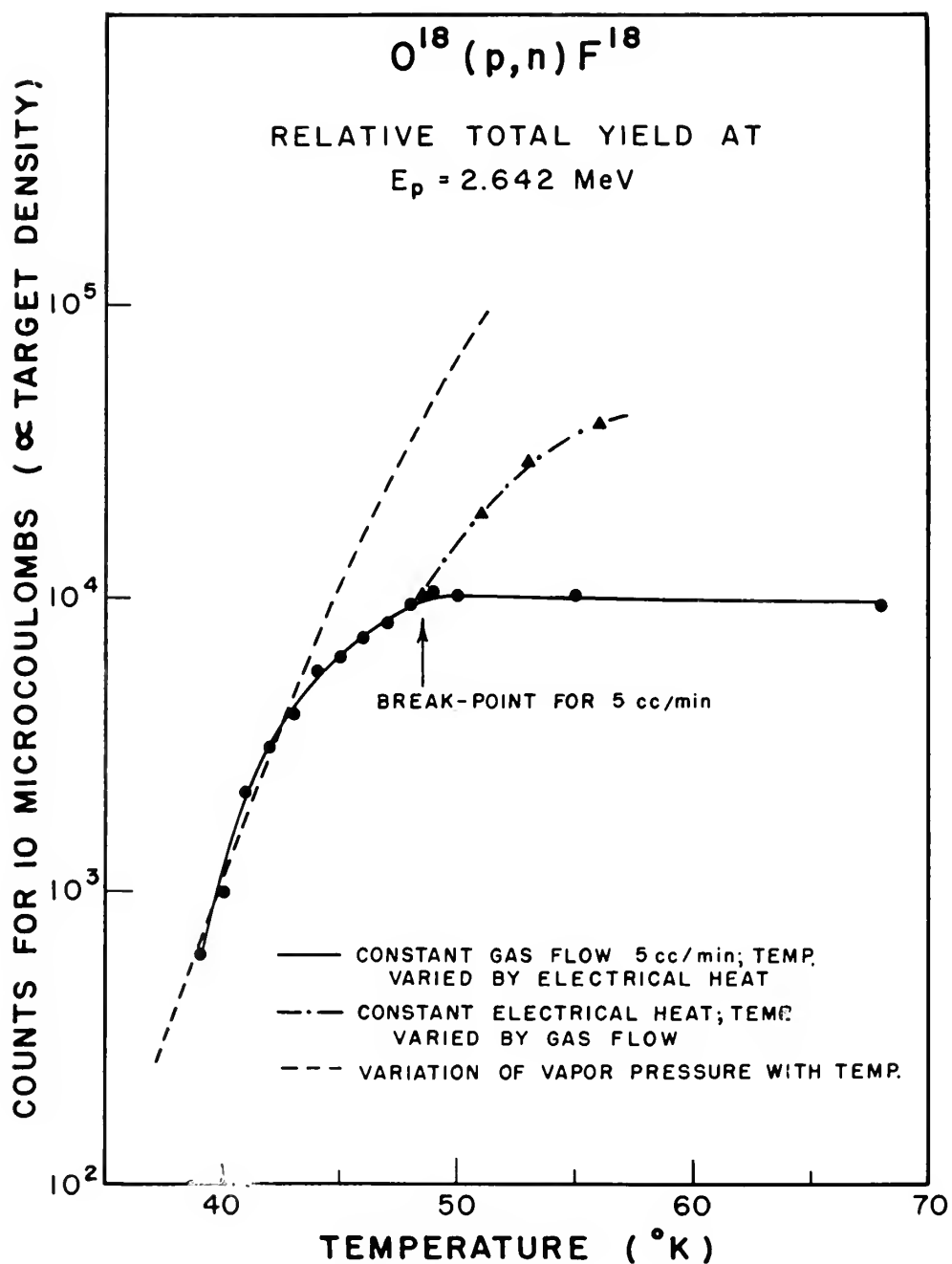
The remaining curve of Figure 22 shows how the target density may be increased for a fixed amount of electrical heating by increasing the input gas flow. Each point on this curve occurs at a temperature which is





Figure 22. Observation of the  $O^{18}(p,n)$  Yield at 2.642 MeV.  
Illustrates the break-point for 5 cc/min.  
input gas flow.







above the break-point for that particular gas flow. This is demonstrated by the data of Figure 23 where a series of electrical heating curves were run on gas flows from 5 to 20 cc/min.. Comparing the curves for 5 and 15 cc/min. it is seen that the break-point for 15 cc/min. lies about three degrees above that for 5 cc/min. as our theoretical escape rate curve would indicate.

There is almost a linear variation of target density with input gas flow as long as the temperature is maintained at or above the break-point of each flow rate considered. This is shown in Figure 24. The limiting factor on target density is imposed by the trapping cylinders which become inadequate for excessively large gas flows, thus spoiling the main system vacuum.

In predicting absolute target density we get an upper limit by assuming the pressure in the inner chamber to be that of the vapor above the condensate at the temperature involved. Of course at the operating temperature we know that there is no condensate and the density must be considerably less than the "vapor pressure" value. Absolute target densities have been difficult to measure experimentally because the cross sections for most of the reactions studied are not well known. However rough measurements on the  $D^2(d,n)He^3$  and  $B^{11}(p,n)C^{11}$  reactions indicated that actual target densities were about a factor of ten less than values based on vapor pressure. For the oxygen gas the measured resolution of the  $O^{18}(p,n)$  neutrons indicated a target density on the order of  $10^{16}$  atoms/cm<sup>2</sup> for a 10 cc/min.





Figure 23. Observation of the  $O^{18}(p,n)$  Yield at 2.642 MeV.  
Illustrates the break-point for various gas flows.

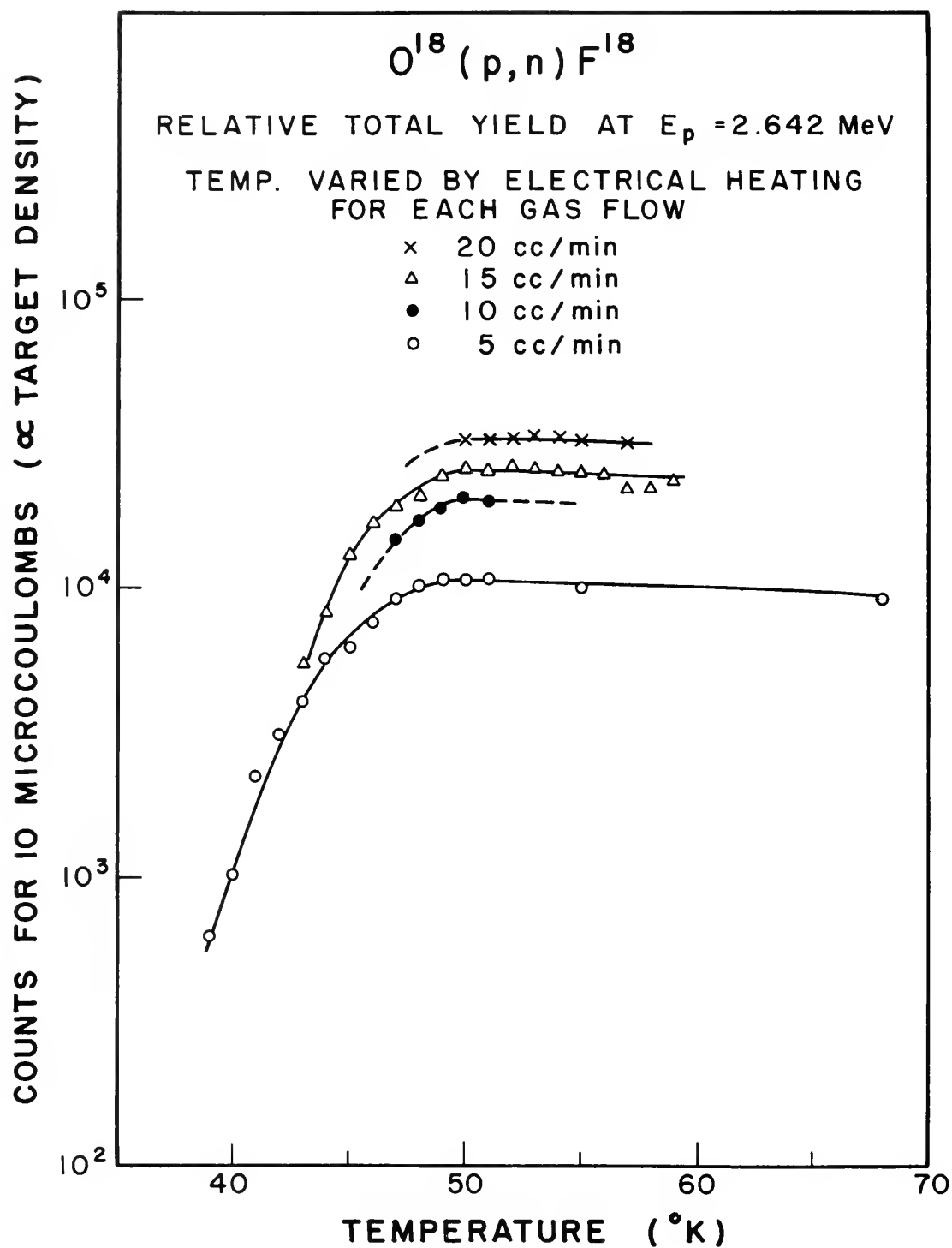
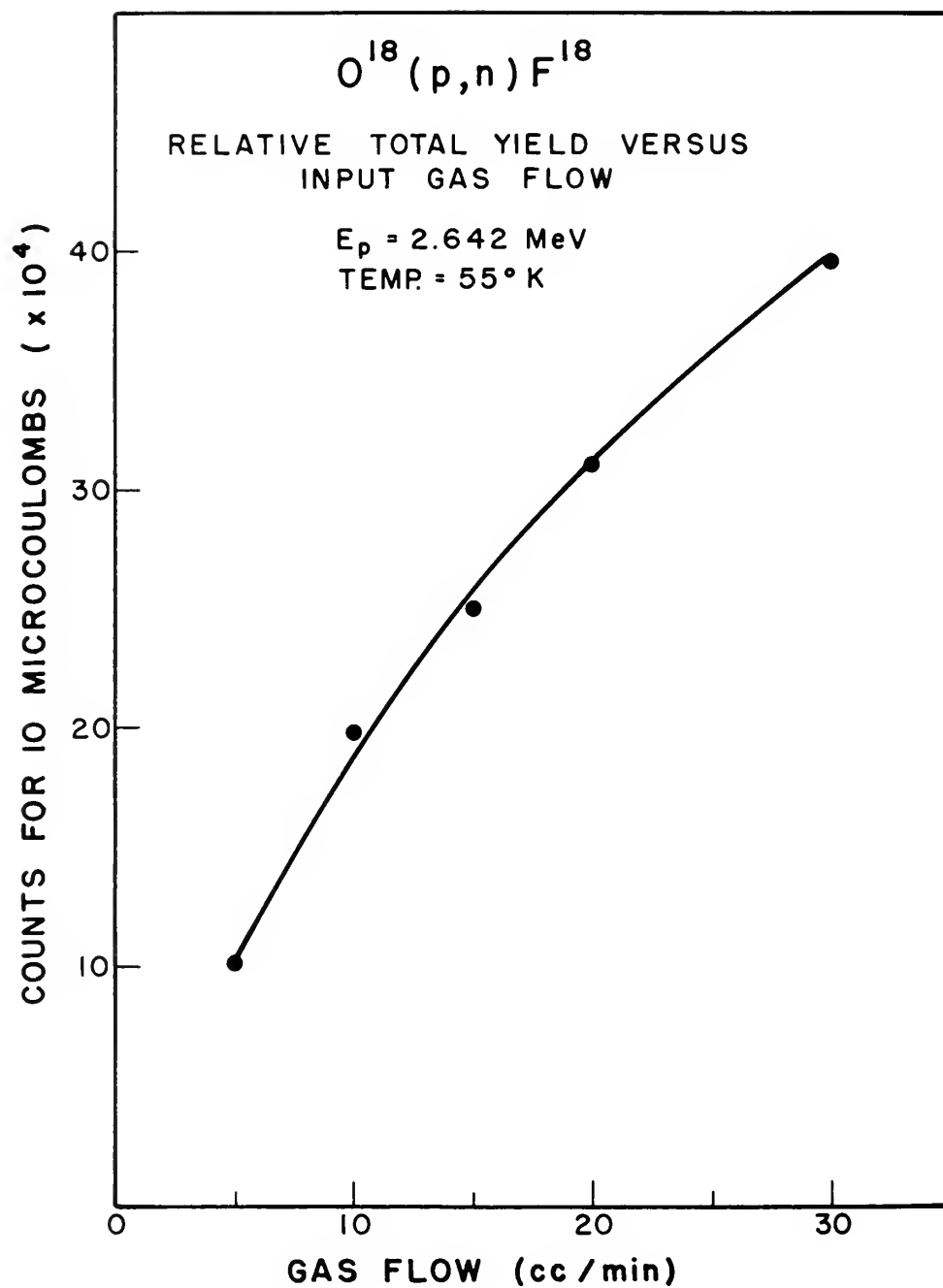








Figure 24.  $\text{O}^{18}(\text{p},\text{n})$  Yield as a Function of Input Gas Flow.  
The temperature ( $55^{\circ}\text{K}$ ) is above the break-point  
of each gas flow considered.





gas flow at 53°K. Again this is an order of magnitude less than the calculated "vapor pressure value" for this temperature. This is also easily seen from Figure 22 where at about 50°K there is an order of magnitude difference between the dashed and solid curves.

Once the operating temperature is predicted, the remaining question of main refrigerant boil-off rate may be answered. Actually this consideration is important only when liquid helium is used. The present main refrigerant container will hold a full charge of two liters of liquid helium. Taking into account all residual heat leaks plus the heat inputs from expected gas flow and electrical heating (including heat applied to the de-icers) a four hour liquid helium lifetime was calculated for a 10 cc/min. oxygen input rate. Experimental results indicated a slightly higher boil-off rate but in reasonable agreement with this estimate.



## APPENDIX C

### NEUTRON ENERGY RESOLUTION CALCULATIONS

This appendix was included to explain in some detail the calculations involved in predicting the various components of the neutron energy distribution. Each component will be discussed separately and shown in Figures 26 and 27 for  $\Theta = 20^\circ$  or  $160^\circ$  respectively.

Since all of the contributing distributions are calculated directly in terms of proton energy with the exception of the angular spread, the ratio  $\Delta E_n / \Delta E_p$  as a function of neutron energy is required. The non-relativistic Q Equation (Eq. 2, p. 52) may be solved for neutron energy as a function of proton energy for a given angle  $\Theta$ . Using the IBM 7072 computer to make this calculation in small energy steps for  $\Theta = 20^\circ$  and  $160^\circ$ , the desired ratios as functions of neutron energy may be determined. Curves of  $\Delta E_n / \Delta E_p$  versus  $E_n$  are shown in Figure 25. Of course for  $\Theta = 20^\circ$  we neglect the region below  $O^{18}(p,n) 90^\circ$  threshold where two energy groups of neutrons are present.

The incident proton energy distribution with a half width of 1/11000







Figure 25.  $\Delta E_n / \Delta E_p$  for  $O^{18}(p,n)$  at  $\Theta = 20^\circ$  and  $160^\circ$

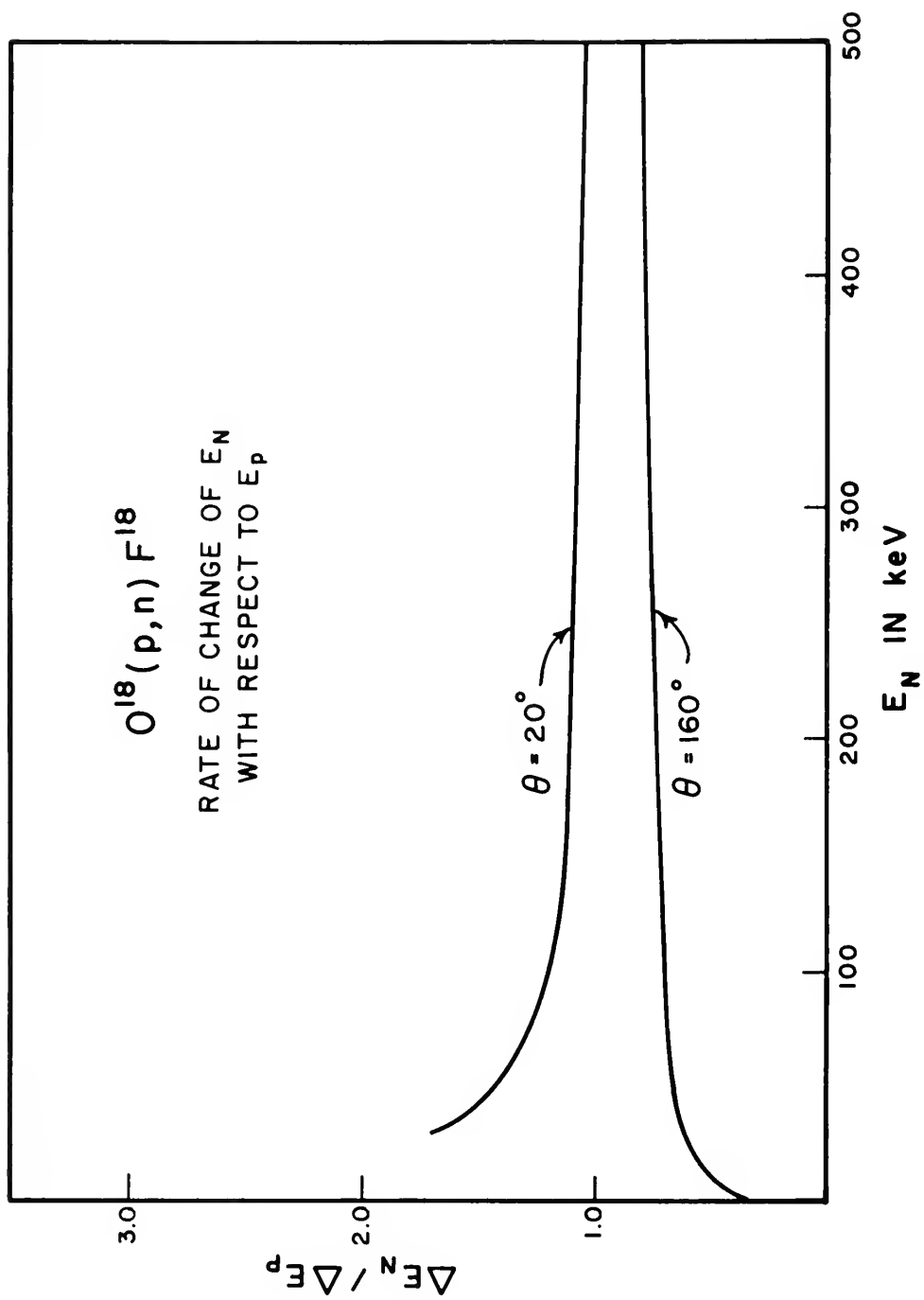






Figure 26.  $O^{18}(p,n)$  Neutron Energy Resolution,  $\Theta = 20^\circ$

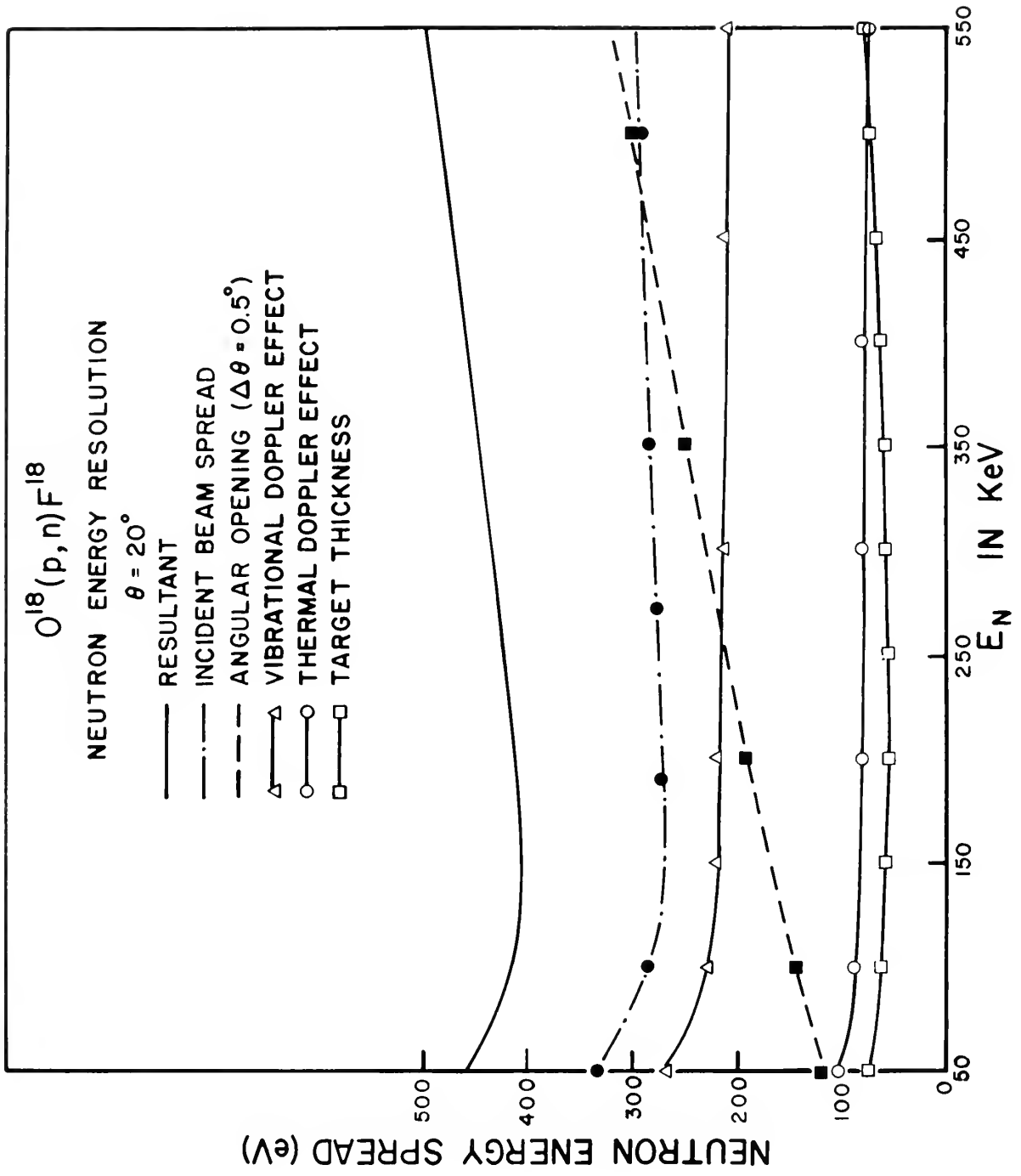
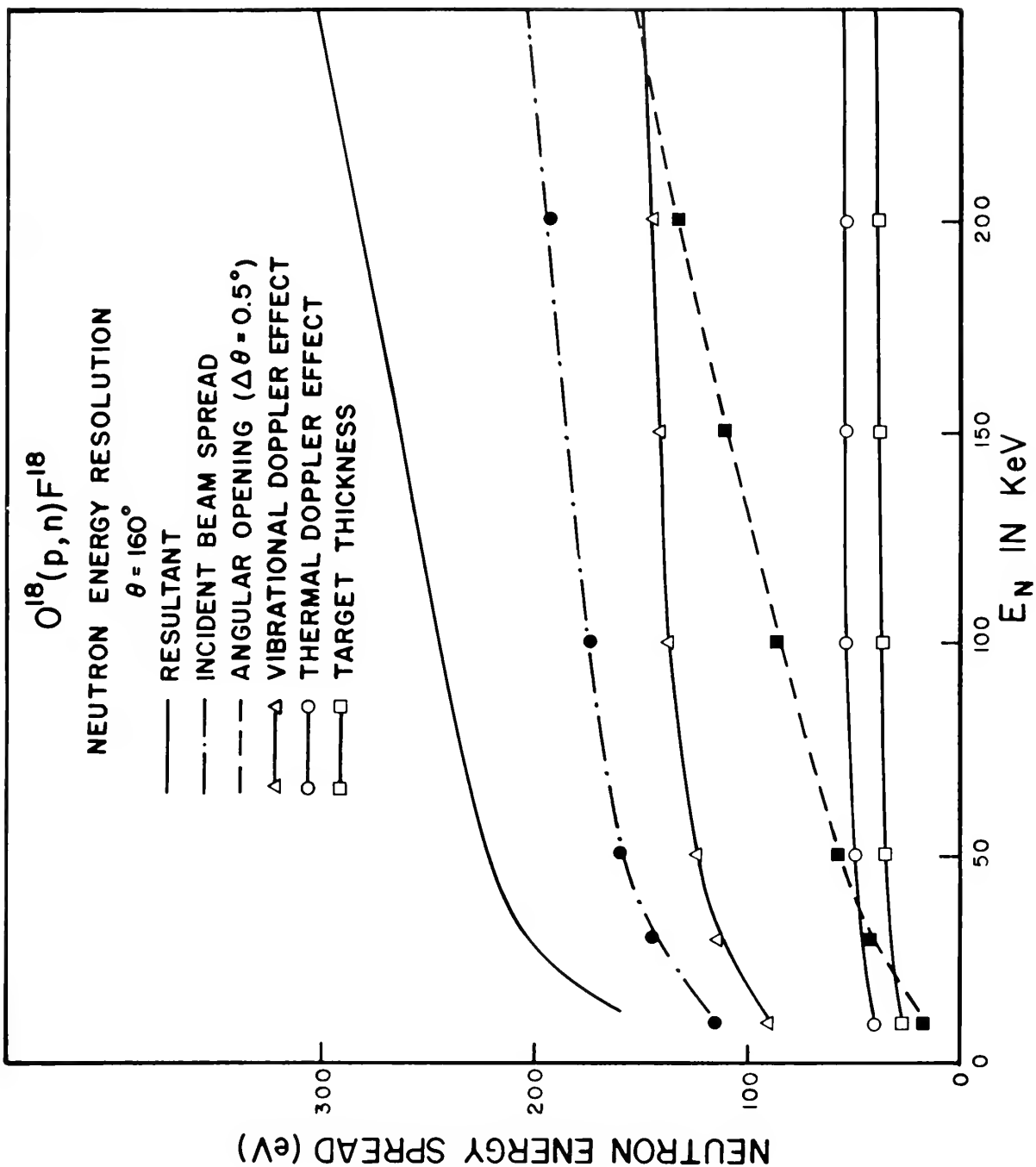








Figure 27.  $\text{O}^{18}(\text{p}, \text{n})$  Neutron Energy Resolution,  $\Theta = 160^\circ$





times  $E_p$  was multiplied by the appropriate  $\Delta E_n / \Delta E_p$  factor to obtain the resultant neutron energy spread contribution appearing in Figures 26 and 27.

In order to obtain  $\partial E_n / \partial \Theta$  we may regard the non-relativistic Q-equation as being in the form  $F(E_n, E_p, \Theta) = 0$ , where  $Q$  is taken as a constant. From the methods of differential calculus we have

$$\left( \frac{\partial E_n}{\partial \Theta} \right)_{E_p} = - \frac{\frac{\partial F}{\partial \Theta}}{\frac{\partial F}{\partial E_n}} .$$

This gives us the form:

$$\frac{\partial E_n}{\partial \Theta} = \frac{2 E_n \sqrt{m_p m_n E_p} \sin \Theta}{\sqrt{m_p m_n E_p} \cos \Theta - (m_n + m_r) \sqrt{E_n}}$$

where  $m_r$  is the mass of the residual nucleus. This expression is much simpler than that derived directly from differentiation with respect to  $\Theta$  of the explicit solution for  $E_n$ . For purposes of illustration, the neutron energy spread,  $\Delta_{\Theta} = \partial E_n / \partial \Theta (\Delta \Theta)$ , was calculated for  $\Delta \Theta = 0.5^\circ$  and the quantity  $.681 \Delta_{\Theta}$  is plotted in Figures 26 and 27. As pointed out in Chapter IV, this quantity is the half width of an equivalent Gaussian distribution.

In calculating the average energy loss of the protons by ionization per unit path length in the target we use the non-relativistic formula (Evans, p. 637, 1955)



$$\frac{dE_p}{dx} = \frac{4\pi z^2 e^4}{m_o v^2} N Z \ln \left( \frac{2m_o v^2}{I} \right) ,$$

where  $m_o$  = electron rest mass,  $V$  = proton velocity,  $N$  = target density,  $Z$  = target atomic number,  $ze$  = proton charge and  $I$  is the geometric-mean excitation and ionization potential for the target atoms. The results of this calculation are, of course, multiplied by our ratio  $\Delta E_n / \Delta E_p$  in order to obtain the equivalent neutron energy spread. The target density was assumed to be approximately  $10^{16}$  atoms/cm<sup>3</sup> for an input gas flow of 10 cc/min. as discussed in Appendix B.

The translational motion of the target atoms introduces a Gaussian Doppler spread in the proton energy (Bethe and Placzek, 1937) whose 1/e width is given by

$$\Delta = 4 \left( \frac{m_p E_p k T}{M} \right)^{\frac{1}{2}}$$

where  $m_p$  = proton mass,  $E_p$  = proton energy,  $T$  = target temperature,  $M$  = target mass and  $k$  = Boltzmann constant. The width at half maximum,  $\Delta_{\frac{1}{2}} = .83 \Delta$ . This Doppler effect is quite small at the temperatures involved in the cryogenic target chamber as seen from Figures 26 and 27.

The final calculation involves the Doppler effect seen by the incident protons due to the vibrational motion of the target atoms in the O<sub>2</sub> molecule. In analogy to the translational Doppler effect we will calculate the half width of the resulting energy distribution function which is also shown to be Gaussian. Only the energy of the ground (zeroth)





vibrational state need be considered since for  $O_2$  the ratio of the number of molecules in the first to that in the ground vibrational state is  $5.74 \times 10^{-4}$  at  $300^\circ K$  (Herzberg, p. 130, 1939). The temperature of the gas in the target chamber is, of course, only around  $50^\circ K$ .

We assume that each atom of the  $O_2$  molecule obeys the linear harmonic oscillator Schrödinger equation (Schiff, p.60, 1955)

$$-\frac{\hbar^2}{2m} \frac{d^2 u}{dx^2} + \frac{1}{2} K x^2 u = E u ,$$

where  $m$  = mass of the atom,  $K$  = oscillator force constant, and  $E$  = energy of oscillation. This equation has solutions

$$u_n(x) = N_n H_n(\alpha x) e^{-\frac{1}{2} \alpha^2 x^2}$$

and eigenvalues  $E_n = (n + 1/2) h \nu$  ,  $n = 0, 1, 2, \dots$  .  $N$  is a normalization constant,  $\nu$  is the classical frequency of oscillation,

$\alpha = (m K / \hbar^2)^{\frac{1}{4}}$  , and  $H_n$  is the  $n^{\text{th}}$  Hermite polynomial. Now we consider only the ground state where  $n = 0$ . Thus we have

$$u_0(x) = \left( \frac{\alpha}{\pi^{\frac{1}{2}} \hbar} \right)^{\frac{1}{2}} e^{-\alpha^2 x^2 / 2}$$

since  $H_0(\alpha x) = 1$ . This can be written in the form

$$u_0(x) = \left( \frac{2m\nu}{\hbar} \right)^{\frac{1}{4}} e^{-\pi m \nu x^2 / \hbar}$$

where

$$\nu = \frac{1}{2\pi} \sqrt{\frac{K}{m}} .$$



Following the treatment of Schiff, p.53 (1955) we can expand  $u_0(x)$  in terms of the normalized momentum eigenfunctions which in infinite space have the form

$$\varphi_k(x) = \left(\frac{1}{8\pi^3}\right)^{\frac{1}{2}} e^{ikx}$$

where  $k = p/\hbar$  and  $p = \text{momentum}$ . Hence we have

$$u_0(x) = \sum_k A_k \varphi_k(x)$$

and

$$A_k = \int_{-\infty}^{+\infty} \varphi_k^* u_0(x) dx.$$

What we want to obtain is the momentum probability function  $P(k) = |A_k|^2$ . Thus we have to evaluate the integral

$$A_k = C \int_{-\infty}^{+\infty} e^{-ikx} e^{-\pi m \nu x^2 / \hbar} dx.$$

This integration has been performed by Elsasser (1933). Following his solution we obtain

$$A_k = C' e^{-\hbar k^2 / 4\pi m \nu}$$

where  $C'$  is a constant  $= \left(\frac{1}{4\pi^3}\right)^{\frac{1}{2}} \left(\frac{\hbar}{2m\nu}\right)^{\frac{1}{4}}$ .

Hence

$$P(k) = |A_k|^2 = (C')^2 e^{-\hbar k^2 / 2\pi m \nu}$$

and we see that the momentum distribution function of the vibrating atom is Gaussian in form with a width at half maximum

$$\Delta p = 2 [2\pi \hbar m \nu \ln(2)]^{\frac{1}{2}}.$$

From this we can calculate the half width of the resultant spread introduced



into the proton energy i.e.,

$$\Delta V = \frac{\Delta p}{m} \quad \text{and} \quad \Delta E_p = \sqrt{2m_p E_p} \Delta V .$$

Thus

$$\Delta E_p = \frac{4}{m} [\pi h \nu m_p E_p \ln(2)]^{\frac{1}{2}} .$$

The classical vibrational frequency  $\nu$  for the  $O^{16}$  molecule is given by Herzberg, p.491 (1939). Assuming the force constant for the  $O^{16}$  and  $O^{18}$  molecules to be the same, the ratio of the vibrational frequencies of the two molecules is inversely proportional to the square root of their masses i.e.,

$$\nu_{O^{18}} = \sqrt{\frac{9}{8}} \nu_{O^{16}} = .943 \nu_{O^{16}} .$$

Thus far we have assumed the axis of vibration to be along the beam axis where the velocity spread experienced by the incident proton would be the full  $\Delta V$  as calculated. However we know that the motion of vibration is actually isotropic in space. Therefore, by averaging the cosine of the angle between the beam and vibrational axes from zero to  $\pi/2$ , we define an average  $\Delta V$  by  $\Delta V_{ave.} = \frac{1}{2} \Delta V$  ; in turn this gives  $\Delta E_{p_{ave.}} = \frac{1}{2} \Delta E_p$  .

In Figures 26 and 27 this average vibrational Doppler effect has been plotted after conversion to neutron energy spread.

The resultant total neutron energy width was predicted by combining the individual widths such that

$$\Delta_{total} = [\sum_i \Delta_i^2]^{\frac{1}{2}}$$

as discussed in Chapter IV.



## LIST OF REFERENCES





## LIST OF REFERENCES

- K.W. Allen and E. Almqvist, Rev. Sci. Instr. 24, 70 (1953).
- H.A. Bethe and G. Placzek, Phys. Rev. 51, 450 (1937).
- E.G. Bilpuch, C.D. Bowman, J.A. Farrell, and H.W. Newson, Ann. Phys. (to be published).
- E.G. Bilpuch, K.K. Seth, C.D. Bowman, R.H. Tabony, R.C. Smith, and H.W. Newson, Ann. Phys. 14, 387 (1961).
- J.M. Blair and J.J. Leigh, Phys. Rev. 118, 495 (1960).
- R.O. Bondelid and J.W. Butler, Nuclear Physics 53, 618 (1964).
- C.D. Bowman, E.G. Bilpuch, and H.W. Newson, Ann. Phys. 17, 319 (1962).
- R.M. Brugger, T.W. Bonner, and J.B. Marion, Phys. Rev. 100, 84 (1955).
- W. Elsasser, Zeitschrift Für Physik 81, 337 (1933).
- R.D. Evans, The Atomic Nucleus (M<sup>C</sup>Graw-Hill, New York, 1955).
- F. Everling, L.A. König, J.H.E. Mattauch, and A.H. Wapstra, Nuclear Physics 18, 529 (1960).
- J.B. Garg, J. Rainwater, and W.W. Havens, Jr., "High Resolution Neutron Spectroscopy in the keV Region: Al, Ti, Fe, Ni, Cu, Zn, V, Mn, Co, and Bi", EANDC (US) - 54 "L", CR - 1860, (1964).
- G. Herzberg, Molecular Spectra and Molecular Structure (Prentice-Hall Inc., New York, 1939).
- H.A. Hill and J.M. Blair, Phys. Rev. 104, 198 (1956).
- C.H. Johnson and H.E. Banta, Rev. Sci. Instr. 27, 132 (1956).
- G.C. Kyker, Jr. and R.M. Williamson, Rev. Sci. Instr. 33, 872 (1962).



- T. Lauritsen and F. Ajzenberg-Selove, *Nuclear Physics* 11, 1 (1959).
- J.B. Marion, *Revs. Mod. Phys.* 33, 139 (1961).
- H. Mark and C. Goodman, *Phys. Rev.* 101, 768 (1956).
- H.W. Newson, private communication (1963).
- H.W. Newson, E.G. Bilpuch, F.P. Karriker, L.W. Weston, J.R. Patterson, and C.D. Bowman, *Ann. Phys.* 14, 365 (1961).
- H.W. Newson, J.H. Gibbons, H. Marshak, E.G. Bilpuch, R.H. Rohrer, and P. Capp, *Ann. Phys.* 14, 346 (1961).
- P.F. Nichols, "High Resolution Neutron Spectroscopy in the Kilovolt Region", unpublished Ph.D. dissertation, Duke University (1958).
- P.F. Nichols, E.G. Bilpuch, and H.W. Newson, *Ann. Phys.* 8, 250 (1959).
- P.B. Parks, "Properties of (p,n) Reactions in Tenuous Gases", unpublished Ph.D. dissertation, Duke University (1963).
- P.B. Parks, private communication (1964).
- P.B. Parks, P.M. Beard, E.G. Bilpuch and H.W. Newson, *Rev. Sci. Instr.* 35, 549 (1964).
- P.B. Parks, H.W. Newson, and R.M. Williamson, *Rev. Sci. Instr.* 29, 834 (1958).
- L.I. Schiff, Quantum Mechanics (M<sup>C</sup>Graw-Hill, New York, 1955).



## BIOGRAPHY

Percy Morris Beard, Jr.

Born: March 31, 1936, Opelika, Alabama

Education:

B.S. U.S. Naval Academy 1958

Positions:

Commissioned Officer, United States Navy 1958 - present

Publications:

Cryogenic System for the Production of Very Thin Targets (with Parks, Bilpuch, and Newson) Rev. Sci. Instr. 35, 549-557 (1964).

Abstracts:

A Windowless Gas Target Chamber Using Cryogenic Techniques (with Parks, Bilpuch, and Newson) Bull. Am. Phys. Soc. 8, 48 (1963).

High Resolution Measurement of the  $A^{40}(p,n)K^{40}$  Relative Cross Section (with Parks, Bilpuch, Farrell, Kyker, and Newson) Bull. Am. Phys. Soc. 8, 48 (1963).

Precision Measurements of the Thresholds of  $Cl^{37}(p,n)A^{37}$  and  $A^{40}(p,n)K^{40}$  Reactions (with Parks, Bilpuch, and Newson) Bull. Am. Phys. Soc. 9, 32 (1964).















thesB29

A High resolution study of the O(18) (p.



3 2768 002 12887 8

DUDLEY KNOX LIBRARY